

Gravity anomalies, flexure and mantle rheology seaward of circum-Pacific trenches

J. Hunter and A.B. Watts

Department of Earth Sciences, South Parks Road, Oxford OX1 3AN, United Kingdom. E-mail: tony@earth.ox.ac.uk

Accepted 2016 July 20. Received 2016 June 28; in original form 2016 April 13

SUMMARY

We have used ensemble averages of satellite-derived free-air gravity anomaly data, together with inverse modelling techniques, to determine the effective elastic thickness, T_e , of circum-Pacific subducting oceanic lithosphere and its relationship to plate age. Synthetic modelling tests show that T_e can be recovered best using gravity anomaly, rather than bathymetry, data and profiles that are at least 750 km long. Inverse modelling based on a uniform T_e elastic plate suggests that T_e increases with age of the subducting oceanic lithosphere and is given approximately by the depth to the $390 \pm 10^\circ\text{C}$ oceanic isotherm based on a cooling plate model. Misfits between the observed and calculated gravity anomalies are significantly improved if a mechanically weak zone is included between the trench axis and the outer rise. This weak zone is coincident with observations of bend-faulting and seismicity. Inverse modelling shows that T_e landward of the outer rise is generally 40–65 per cent less than the T_e seaward of the outer rise. Both landward and seaward T_e increases with age of the lithosphere and are given by the depth to the $342\text{--}349^\circ\text{C}$ and $671\text{--}714^\circ\text{C}$ oceanic isotherm, respectively. A dependence of T_e on age is consistent with models for the cooling of oceanic lithosphere as it moves away from a mid-ocean ridge and the temperature-dependent ductile creep of oceanic lithospheric minerals such as olivine. By comparing the observed T_e to the predicted T_e based on laboratory-derived yield strength envelopes and an assumption of elastic-perfectly plastic deformation, we have attempted to constrain the rheology of oceanic lithosphere. Regardless of the assumed friction coefficient, the dry-olivine low-temperature plasticity flow laws of Goetze, Evans & Goetze, Raterron *et al.* and Mei *et al.* all provide quite a good fit to the observed T_e at circum-Pacific subduction zones. This result contrasts with the Hawaiian Islands, where these flow laws are generally too strong to fit the observations. The discrepancy in rheology within Pacific plate may be caused by differences in the timescale of loading and therefore the amount of viscoelastic stress relaxation that has occurred. Other possibilities include thermal rejuvenation and magma-assisted flexure at the Hawaiian Islands.

Key words: Gravity anomalies and Earth structure; Subduction zone processes; Lithospheric flexure; Rheology: mantle; Pacific Ocean.

1 INTRODUCTION

Plate tectonics is based on the assumption that Earth's outermost layer, or lithosphere, is rigid and capable of supporting loads such as ice sheets, volcanoes and sediments for long periods ($>10^6$ a) of geological time. The pioneering studies of Gilbert (1890) and Barrell (1914) suggest many such loads are regionally, rather than locally, compensated by flexure. Since then, Jeffreys (1926), Vening Meinesz (1941), Gunn (1943), Walcott (1970) and others have successfully modelled the lithosphere as an elastic plate overlying an inviscid substrate and used it to explain bathymetry/topography, gravity and seismic observations in the region of oceanic islands, mountain ranges, river deltas and deep-sea trench-outer rise systems.

The elastic plate model predicts that the flexural depressions caused by downward acting loads are flanked by an uplift, variously referred to as a peripheral bulge or outer rise. Walcott (1970) first pointed out the existence of such a bulge seaward of the Kuril Trench in the northwest Pacific Ocean (the Hokkaido rise) in Scripps Institution of Oceanography bathymetry maps. Subsequently, Hanks (1971) showed that the depth of the trench below the regional seafloor depth could be explained by a broken (i.e. semi-infinite) elastic plate, or flexure, model with a vertical shear force applied at the trench axis and an effective elastic plate thickness, T_e , of 27 km. He argued for a large horizontal compressive force on the edge of the plate in order to fit the steep seaward wall of the trench and to account for a thrust-faulting outer-rise earthquake.

Watts & Talwani (1974) demonstrated that a flexure model was in accord with the observed free-air gravity anomaly seaward of trenches, which showed a positive correlation with topography of ~ 90 mGal km $^{-1}$, consistent with crustal warping. These authors fixed T_e and varied the vertical shear and horizontal forces acting at the plate break until a satisfactory fit had been obtained with shipboard gravity and topography data. Caldwell *et al.* (1976) modelled trench-outer rise bathymetry in the northern and western Pacific using an elastic plate loaded by an applied bending moment and vertical shear force. They devised a method in which T_e , together with the end-loads, could be estimated by measuring the height and width of the outer rise, finding little T_e variation with values of 20–29 km. This study, together with a subsequent one by Parsons & Molnar (1978), showed that when an applied bending moment is considered, large horizontal stresses were not required to fit observations seaward of trenches.

The T_e deduced by Hanks (1971) seaward of the Kuril trench, together with estimates from topographic loads at the Hawaiian-Emperor Seamount chain and the East Pacific Rise crest (Cochran 1979), were used by Watts (1978) to argue that oceanic T_e depends on the age of the lithosphere at the time of loading and does not change appreciably with time. In light of these results, Caldwell & Turcotte (1979) re-examined shipboard bathymetry data seaward of circum-Pacific subduction zones and showed that young lithosphere at the Middle America trench has a lower T_e and is therefore much weaker than older lithosphere at the western Pacific trenches.

Whilst the elastic plate model fit bathymetry data well, there were exceptions, most notably in the region of the seaward wall of the trench. A further difficulty, as pointed out by De Bremaecker (1977), is that the elastic model, unlike viscous models, predicts unreasonably high bending stresses (up to 900 MPa) in the outermost portions of the flexed plate. These observations led McAdoo *et al.* (1978) and Bodine & Watts (1979) to use an elastic-perfectly plastic plate rather than an elastic one, where the yield stress was assumed to be either independent of depth or vary linearly with depth.

Goetze & Evans (1979) proposed the Yield Strength Envelope (YSE), which defined, for the first time, the expected variation of yield stress with depth based on laboratory-derived failure criteria for brittle and ductile deformation of oceanic mantle-type rocks. This development allowed Bodine *et al.* (1981), McNutt & Menard (1982), McAdoo *et al.* (1985) and Judge & McNutt (1991) to model the deep sea trench-outer rise system using an elastic-plastic plate with a depth-dependent yield stress. In addition, under the assumption of perfectly plastic yielding, YSEs could be used along with observed plate curvatures to predict T_e , which could then be compared with T_e estimates obtained by modelling gravity and bathymetry data.

The linearly elastic plate model is a simple one that makes it conducive to parameter search and inversion techniques. Levitt & Sandwell (1995), for example, performed a joint inversion of satellite-derived free-air gravity anomaly and ship track bathymetry profiles seaward of subduction zones, inverting for parameters such as flexural amplitude and wavelength, trench axis location, and applied bending moment. They found that while younger (<80 Ma) lithosphere is clearly weaker than older (>80 Ma) lithosphere, there is scatter in the relationship between T_e and oceanic plate age, particularly for older lithosphere, which they variously attributed to noise in the bathymetry data and inelastic yielding.

A relationship between oceanic T_e and plate age is not surprising. Variations of heat flow and bathymetry suggest that oceanic lithosphere behaves as a cooling plate, subsiding and increasing its depth

following its creation at a Mid-Ocean Ridge (MOR) system (Parsons & Sclater 1977). Furthermore, laboratory deformation studies of oceanic mantle minerals such as olivine show that at relatively high temperatures, they deform by temperature-dependent creep, and their flow strength is inversely related to temperature (Karato *et al.* 1993). It follows therefore that oceanic lithosphere should strengthen with age as it moves away from the MOR and there is strong evidence from volcanic loads at seamounts and oceanic islands (e.g. Watts 1978) that this is indeed the case.

Despite the possibility of significant inelastic yielding and faulting seaward of the trench (Jones *et al.* 1978; Masson 1991; Ranero *et al.* 2003, 2005; Billen & Gurnis 2005) and dynamic effects, due for example to the dense downgoing slab and its regional compensation (Watts & Talwani 1975), the outer rise seaward of trenches should, in principle, be one of the best places to examine oceanic plate flexure and its relationship to age. This is because outer rise oceanic lithosphere is not subject to the thermal and mechanical ‘overprint’ that may characterize the lithosphere that underlies volcanic loads, for example, at seamounts and oceanic islands.

Somewhat surprisingly therefore, Bry & White (2007) found no relationship between oceanic T_e and plate age seaward of circum-Pacific deep-sea trenches. This was the first such study to use high-resolution grids of bathymetry and satellite-derived gravity, to construct averaged profiles to reduce noise, to estimate errors by calculating the misfit as a function of T_e , and to use inversion techniques to derive the applied forces at the trench axis. More recently, Contreras-Reyes & Osses (2010) found only a weak correlation between T_e and plate age using high-resolution bathymetry grids and seismic reflection profiles at the Peru–Chile trench-outer rise system (0–50 Ma). Both authors, however, recognized that plate-weakening seaward of the trench may have influenced their conclusions regarding the dependence of T_e on age.

The purpose of this paper is to present the results of a new flexural analysis of free-air gravity anomaly data seaward of circum-Pacific trenches using an inversion technique that takes into account spatial variations in T_e both across and along the outer rise. We use the inversion results to re-examine the relationship between T_e and oceanic plate age, and compare our results to previous studies, including that of Bry & White (2007). We then use our T_e results to constrain parameters in laboratory-derived flow laws for olivine, including laws for low temperature plasticity, and compare our results to those of recent studies of oceanic mantle rheology based on volcano loading in the interior of the Pacific plate.

2 GRAVITY DATA

We focus this study on the deep-sea trench-outer rise systems of the circum-Pacific Ocean (Fig. 1) because they reflect a wide range of oceanic plate age, ranging from 2–27 Ma (Middle America) to 140–157 Ma (Mariana), and most have a well-developed outer rise. The outer rise is sometimes characterized by significant topography, such as seamounts, rises and fracture zone ridges and troughs, the effect of which we have attempted to minimise. First, regions of very rough topography were excluded, for example, at the Cocos Ridge (Middle America trench), the Carnegie and Nazca Ridges (Peru trench), the Emperor seamount chain (intersection of the Kamchatka and western Aleutian trenches), the Louisville Ridge (Tonga-Kermadec trench). Also excluded were regions of high sediment-flux, for example at the Cascadia subduction zone and south of the Juan Fernandez Ridge at the Chile trench (Contreras-Reyes & Osses 2010).

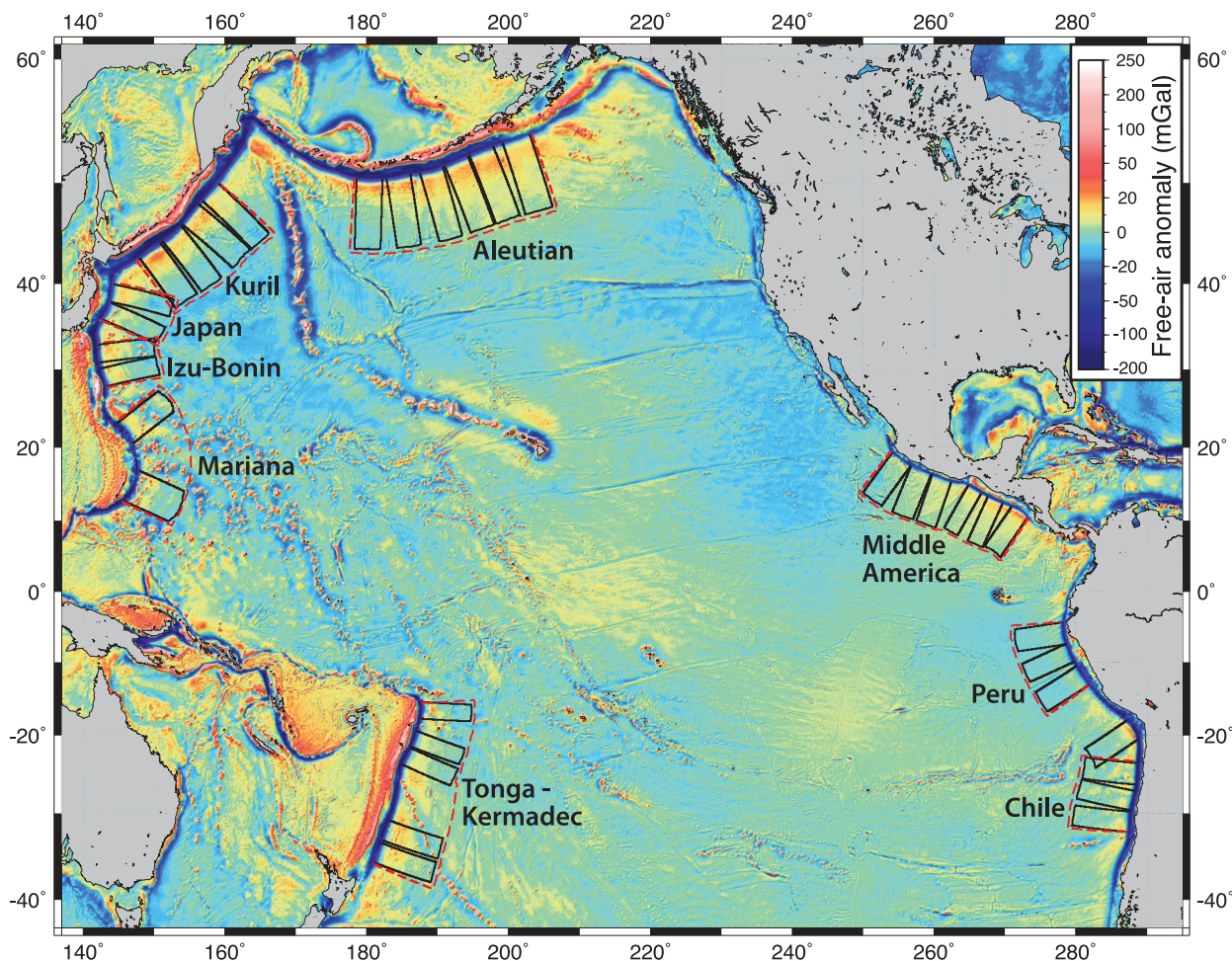


Figure 1. Free-air gravity anomaly map of the Pacific Ocean (Sandwell *et al.* 2014, v23.1), showing the locations of the geographic bins within which the ensemble-averaged profiles were calculated. The red dash shows the 'trench-bins' and the solid black the 'segment-bins'.

Second, we used a 1×1 min global gravity grid (Sandwell *et al.* 2014, v23.1) to construct ensemble-averaged profiles of the free-air gravity anomaly in a number of 'bins' along each deep-sea trench-outer rise system.

To calculate the ensemble-averaged profiles, a series of trench-normal profiles of free-air gravity were sampled within each bin. The frequency spectrum of each profile was then computed using a fast Fourier transform (FFT), the spectra were averaged, and an inverse FFT used to convert the average power spectrum to an average profile in the spatial domain (e.g. Bassett & Watts 2015). Tests show that for ensembles of >30 profiles, which is the case for all bins in this study, spectral and arithmetic techniques yield near identical average profiles (fig. S1 in Bassett & Watts 2015). We used two bin sizes: large bins (trench-bins) that encompass entire trenches (red dash in Fig. 1) and smaller bins (segment-bins) that subdivide each trench into segments (solid black in Fig. 1).

Fig. 2 shows free-air gravity anomaly profiles seaward of the Tonga-Kermadec trench. The figure illustrates that ensemble-averaging successfully suppresses the gravity effect of bathymetric features that are not common to each profile and enhances those that are. For example, the relatively short wavelength gravity anomalies associated with the NW-SE trending Louisville Ridge (LR) seamount chain are almost eliminated from the final ensemble, while the relatively long-wavelength gravity anomalies associated with the outer rise are enhanced.

In order to isolate the gravity effect of the trench-outer rise flexure from other contributions, we made two corrections to the observed free-air gravity anomaly data. Gravity data were corrected for the effect of thermal cooling of oceanic lithosphere away from the MOR (Parsons & Sclater 1977). The geoid height-age relationship for a plate cooling model (Sandwell & Schubert 1980) was first used to calculate the geoid height from the 2×2 min age grid of Müller *et al.* (2008, v3.2). The geoid height was then converted to a gravity anomaly using a Fourier transform transfer function technique (Chapman 1979).

The observed free-air gravity anomaly was also corrected for the gravity anomalies associated with the subducting lithosphere. It has been known for some time that circum-Pacific subduction zones are dominated by long-wavelength positive free-air gravity anomalies that are associated with the dense downgoing slab and its regional compensation (Griggs 1972; Watts & Talwani 1975; Davies 1981). These anomalies are most apparent in spherical harmonic expansions of Earth's gravity field at degree and order in the range 2–16 (i.e. wavelengths ≥ 2500 km). Since the diagnostic wavelength of oceanic plate flexure is $< \sim 1000$ km (Watts & Ribe 1984), these long-wavelength anomalies are unlikely to be supported by the strength of the lithosphere. Therefore, we removed EGM2008 (Pavlis *et al.* 2012) coefficients up to and including degree and order 16 from the observed free-air gravity anomaly prior to analysis.

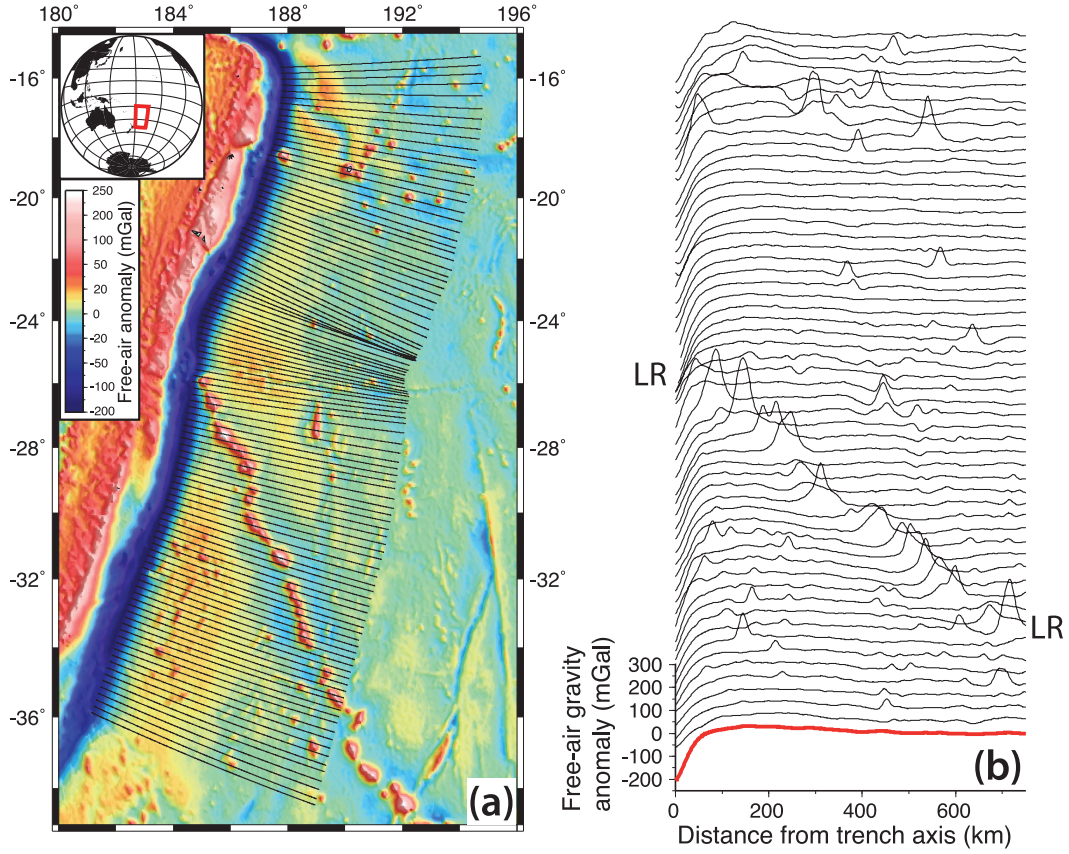


Figure 2. Figure illustrating the calculation of the trench-bin ensemble-averaged gravity profile at the Tonga-Kermadec trench. (a) Free-air gravity anomaly map (Sandwell *et al.* 2014, v23.1) with the locations of the profiles that were ensemble-averaged. (b) The black lines show the free-air gravity along the profiles shown in Fig. 2(a) (for clarity, only every other profile is shown), and the red line shows the ensemble-averaged profile. LR, Louisville Ridge.

Fig. 3 shows trench-bin ensemble-averaged profiles of free-air gravity and bathymetry that have been stacked on the local trench axis, defined as the deepest point in the trench, with the youngest circum-Pacific subducting oceanic lithosphere on top and oldest on the bottom. Interestingly, the figure appears to show a general increase in the flexural wavelength and amplitude of the outer rise with lithospheric age, suggesting that T_e might increase with age. For example, the wavelength of the gravity anomalies associated with the trench-outer rise system is ~ 200 – 250 km at the Middle America and Peru-Chile trenches, ~ 300 – 400 km at the Aleutian and Tonga-Kermadec trenches, and ~ 400 – 500 km at older trenches. This coincides with an increase in the amplitude of the outer rise gravity anomaly, from <16 mGal at the Middle America and Peru-Chile trenches to up to 40 mGal at old (>80 Ma) trenches.

3 FLEXURE AND GRAVITY MODELLING

Flexure of the lithosphere is commonly modelled as a thin elastic plate overlying an inviscid substrate (e.g. Watts 2001). Thin plate theory implies cylindrical bending and flexures that are small relative to the radius of curvature.

We assume here a 2-D elastic plate and a coordinate system such that the x direction is perpendicular to the trench axis, z is parallel to it, and y is normal to the surface of the plate (Fig. 4). The fourth-order differential equation for the flexure of a 2-D elastic plate

overlying an inviscid substrate is given by (e.g. Turcotte & Schubert 1982):

$$\frac{d^2}{dx^2} \left(D(x) \frac{d^2 w}{dx^2} \right) + F \frac{d^2 w}{dx^2} + (\rho_m - \rho_w) g w = q(x), \quad (1)$$

where w is the flexure, F is the axial horizontal force, g is the gravitational acceleration, ρ_m and ρ_w are the densities of the material underlying and overlying the flexed plate, respectively, $q(x)$ is an applied surface load, and D is the flexural rigidity:

$$D = \frac{T_e^3 E}{12(1 - \nu^2)}, \quad (2)$$

where E is Young's modulus and ν is Poisson's ratio. The bending moment, M , and vertical shear force, V , in the flexed plate are given by:

$$M = -D \frac{d^2 w}{dx^2} = D\kappa \quad (3)$$

$$V = \frac{dM}{dx} - F \frac{dw}{dx}, \quad (4)$$

where κ is the plate curvature. To solve eq. (1) for the case of a broken elastic plate, the boundary conditions are as follows:

$$w \rightarrow 0 \text{ as } x \rightarrow \infty$$

$$\frac{dw}{dx} \rightarrow 0 \text{ as } x \rightarrow \infty$$

$$M|_{x=0} = M_o$$

$$V|_{x=0} = V_o, \quad (5)$$

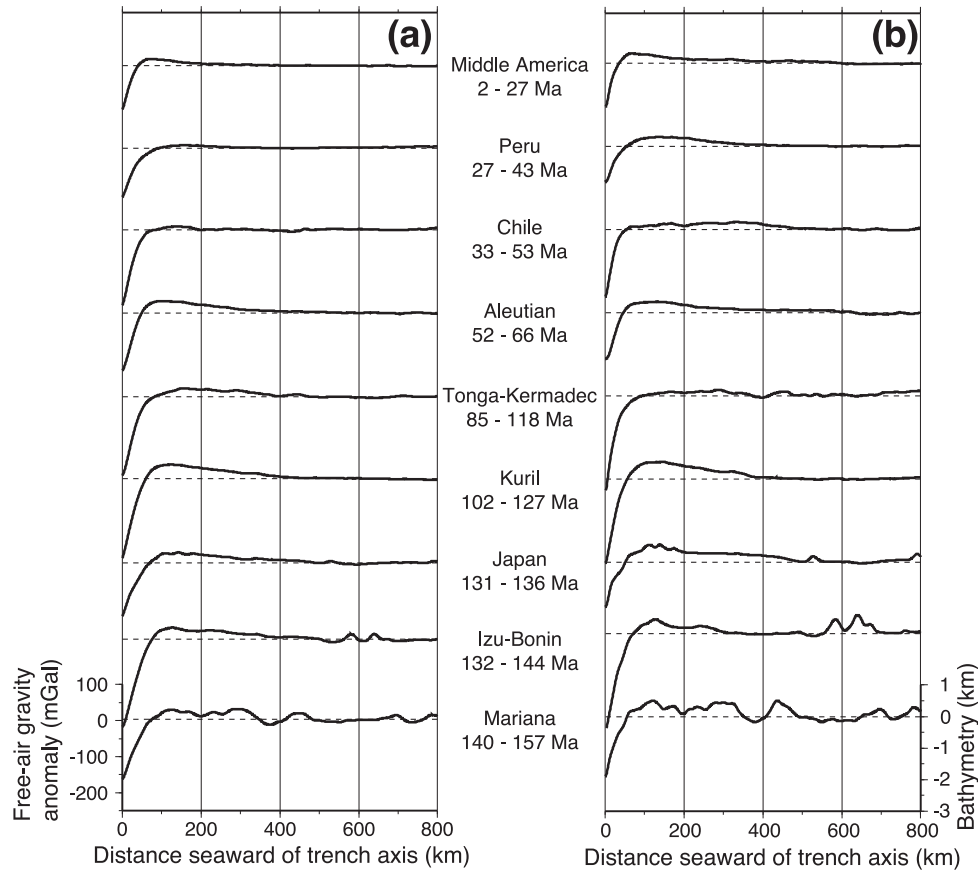


Figure 3. Corrected trench-bin ensemble-averaged profiles of (a) free-air gravity and (b) bathymetry, ordered from top to bottom with increasing age of the subducting plate. The bathymetry profiles have been corrected for the effect of seafloor cooling using the plate cooling model of Parsons & Sclater (1977).

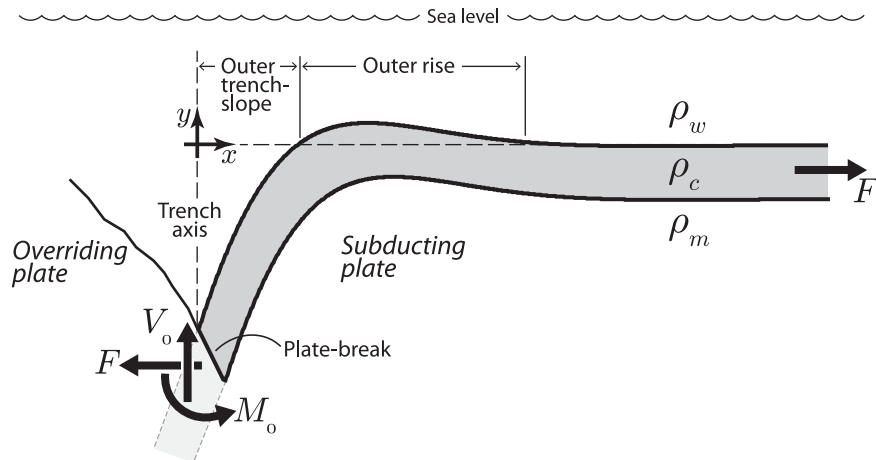


Figure 4. Schematic diagram illustrating the semi-infinite (broken) elastic plate model as applied at a trench-outer rise system. The plate break is located at the trench axis, where a bending moment M_0 and vertical shear force V_0 are applied.

where M_0 and V_0 are the bending moment and vertical shear force applied at the plate break, which we place at the trench axis (Fig. 4). Physically, M_0 and V_0 are the moment and shear force that exist in the lithospheric plate at the trench axis due to tectonic forces such as slab pull, collision resistance, slab suction, and arc volcano and forearc crust loading. These end-loads account for the fact that we are modelling a continuous lithospheric plate with a broken plate.

We follow Contreras-Reyes & Osses (2010) here and use a finite difference approximation to solve eq. (1) for the flexure of a broken plate. This approximation allows horizontal and vertical loading

as well as lateral variation in flexural rigidity to be considered. We tested the approximation against the analytical solution for a uniform T_e broken plate (Turcotte *et al.* 1978), and found a rms error (RMSE), as a percentage of the maximum deflection, of $<10^{-4}$ per cent.

We accounted for seafloor sediments by including a distributed sediment load, ensemble-averaged from the observed sediment thickness grid of Divins (2003), in the flexure calculation. However, tests show that sediment loading has negligible effect on the results of our analysis. The gravity effect of the surfaces of

flexure, including the mantle and crust, crust and sediment, and sediment and water boundaries, were computed using the line integral method of Bott (1960).

4 INVERSION TECHNIQUE

In order to determine T_e directly from gravity observations, we used an inversion technique in which T_e was iterated in steps of 1 km and M_0 , V_0 , and a vertical shift parameter, c , were optimized at each iteration. We found that this technique yielded a robust estimate of T_e and its associated errors. Optimization parameters were found using MPFIT (Markwardt 2009), a damped least squares algorithm based on the MINPACK program (Moré 1978). This seeks the parameters that minimize the objective function:

$$F_{obj}(\beta) = \sum_{n=1}^N [\Delta g_n - \Delta \hat{g}_n(\beta)]^2, \quad (6)$$

where $\beta = (M_0, V_0, c)$ are the optimization parameters, Δg_n and $\Delta \hat{g}_n(\beta)$ are the observed and calculated free-air gravity anomaly, respectively at the n th point in the profile, and N is the number of points in the profile. We choose to present results as an RMSE:

$$\Delta g_{rms} = \sqrt{\frac{F_{obj}}{N}}. \quad (7)$$

By inverting for T_e , M_0 , V_0 and c only, we have ignored the axial compressional or tensional loading term, F in eq. (1). This is reasonable given that trench-outer rise inversions are strongly biased towards tensional axial forces, in accord with the results of Mueller & Phillips (1995), but that the maximum net slab pull force expected to occur, $6 \times 10^{12} \text{ Nm}^{-1}$ (Schellart 2004; Capitanio *et al.* 2009), has little effect on surface elastic plate deflections.

It is desirable when inverting geophysical data to try and constrain as many of the variable parameters as possible prior to inversion. Such constraints reduce computation time and increase the resolution of the recovered T_e . For example, the bending moment, M_0 , generated in a flexed elastic plate is proportional to the radius of curvature of bending. Therefore, observations of the curvature of the subducting plate near the trench axis may be used to constrain M_0 . Unfortunately, it is difficult to estimate curvature directly from bathymetry, as it is sensitive to small fluctuations in seafloor depth. However, observations of seismicity and faulting, seismic imaging, and synthetic testing all suggest that the curvature at the trench axis, and therefore M_0 , is positive; that is that the subducting plate is bent convex upwards and the shallow part of the plate is in tension.

The outer trench-slope, for example, commonly displays normal faulting and seismicity (Appendix A; Jones *et al.* 1978; Masson 1991; Kobayashi *et al.* 1998; Ranero *et al.* 2003, 2005). Swath bathymetry data reveals that the outer trench-slope is, in general, pervasively fractured by normal bend-faults that are parallel or subparallel to the trench axis (Appendix A). A few thrust faults have been observed seaward of some trenches (e.g. Peru–Chile, Tonga–Kermadec), but these are probably normal faults that have been reactivated when they meet the resistance of the overriding plate (Massell 2002). Seismicity studies (Chapple & Forsyth 1979; Christensen & Ruff 1988; Craig *et al.* 2014) reveal that shallow normal-faulting earthquakes are ubiquitous features of the outer trench-slope, extending to depths of up to 30 km. Compressional events are less common and generally occur at greater depths, separated from tensional events by a thin aseismic elastic core (Seno & Yamanaka 1996), again in accord with the predictions of the plate flexure model. There are few observations of intraslab seismicity

immediately landward of the trench axis, but shallow tensional events at the Middle America (Ranero *et al.* 2005), Southern Chile (Tilmann *et al.* 2008), Central Aleutian (Frohlich *et al.* 1982), and Japan (Yoshii 1979) trenches all suggest that the uppermost part of the oceanic lithosphere remains in extension immediately following subduction at the trench.

These studies, together with seismic imaging (as compiled by Hayes *et al.* 2012, for example, in Slab1.0), indicate to us that the subducting oceanic plate is convex up in the vicinity of the trench axis and outer rise. The subducting plate increases its dip from a few degrees at the seaward wall of the trench, to 10–20° along the plate interface, to 30–65° at depths of 75–100 km below sea level (e.g. Isacks & Barazangi 1977). As the curvature is the first derivative of the slope, the lithosphere therefore has positive curvature from the outer rise until intermediate earthquake depths.

Finally, synthetic tests suggest that M_0 is likely to be positive. For example, we loaded a broken (i.e. semi-infinite) plate with a trapezoidal end load to simulate the overriding plate and a bending moment to simulate the dense downgoing slab. The plate curvature at the leading edge of the trapezoidal load (i.e. the trench axis) was then calculated for a range of load heights and widths, applied bending moments and axial loads, and T_e . We conducted tests with plates of constant rigidity and a rigidity that decreased landward of the outer rise. In total, 540 tests were run, and in all cases the curvature at the trench axis, and therefore M_0 , was positive.

Unfortunately, it is not possible to constrain the other parameters. For example, V_0 may be either negative or positive. This is because V_0 is proportional to the area bounded by the surface of flexure, and visual inspection of ensemble-averaged bathymetry profiles suggests that this area is positive at some trenches and negative at others. In addition, it has been suggested that at some trenches, the point of maximum bending moment occurs 20–50 km seaward of the trench axis and the plate starts to unbend landward of this point, whilst at other trench systems it occurs landward of the trench axis (Watts & Talwani 1974; McAdoo *et al.* 1978; Bodine & Watts 1979; Chapple & Forsyth 1979; Contreras-Reyes & Osses 2010).

5 SYNTHETIC MODELLING

To test the efficacy of our inversion methodology, we generated synthetic profiles of both bathymetry and gravity based on certain parameters and then inverted them to see how well the input T_e could be recovered.

The first step was to create a typical trench-outer rise flexure profile using eqs (1) and (5). Two sets of profiles were produced. The first set was calculated with plates of uniform rigidity; 80 of these profiles were produced with T_e in the range 10–80 km. The second set was calculated with variable rigidity plates that weaken landward of the outer rise; this was to simulate any bending-induced plate weakening (e.g. Bodine & Watts 1979; Goetze & Evans 1979; Contreras-Reyes & Osses 2010). The end-loads used to calculate the flexure were chosen semi-randomly to give trench depths that are in the range of those observed.

The second step was to add noise to the typical profile in order to simulate short wavelength features on the outer rise such as seamounts, fracture zones, abyssal hills and other topography (Appendix B).

The third step was to simulate the landward wall of the trench. At some trenches, low-density sediments beneath the landward wall contribute to the gravity anomaly over the outer trench-slope and also shifts the minimum of the gravity anomaly landward of the

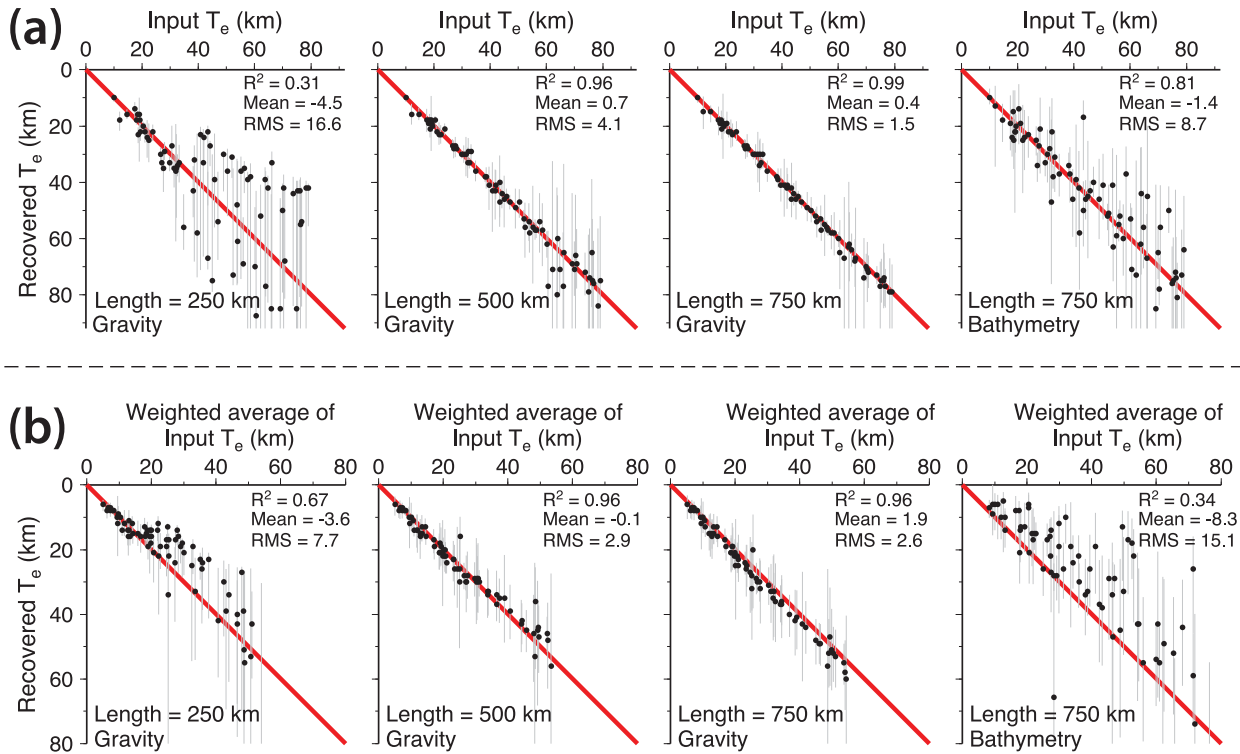


Figure 5. Results from inversion of synthetic trench-outer rise profiles, showing the effect of varying profile length and data type (labelled on each plot). Also labelled on each plot is the R^2 value, and the mean and rms difference between the input and recovered T_e . (a) Results from inversion of the uniform rigidity synthetic profiles. (b) Results from inversion of the variable rigidity synthetic profiles; the input T_e is given as a weighted average of the input T_e profile, with weights determined by the squared magnitude of the input gravity anomaly.

bathymetric minimum (Hayes & Ewing 1970; Talwani 1971; Watts & Talwani 1974). As our broken elastic plate model does not account for the landward side of the trench, it was important to test if this has an effect on the accuracy of the modelled T_e . We therefore simulated a low-density landward wall in the synthetic profiles, with steepness ~ 2 times that of the synthetic outer-trench slope, as assessed by analysis of observed ensemble-averaged bathymetry profiles, and density of 2400 kg m^{-3} .

The final step was to calculate the free-air gravity anomaly associated with the synthetic profile, taking into account bathymetric noise, the flexed top and base of the oceanic crust, and the landward wall of the trench. The noise was assumed to be isostatically compensated assuming a low $T_e = 5\text{--}15 \text{ km}$, which is reasonable given the fact that many of the short wavelength bathymetric features on the outer rise form part of the tectonic fabric of the oceanic crust and so were generated at a MOR. A mean crustal thickness of 6 km was used, and the mean water depth was semi-randomly chosen to reflect the range of seafloor depths of the subducting plate.

Fig. 5 shows the input T_e used to generate the synthetic bathymetry and free-air gravity anomaly profiles compared to the T_e recovered from inversion. The top and bottom panel shows results from inversion of the uniform T_e and variable T_e synthetic profiles, respectively. The figure shows that the inversion of synthetic gravity better recovers the input T_e than does inversion of synthetic bathymetry. The main reason for this is that both isostatic compensation and upward continuation act to reduce the gravity anomaly associated with short wavelength bathymetry, and therefore there is less masking of the trench-outer rise signal in the gravity data than in the bathymetry data. Indeed, Fig. 5 shows that the T_e recovery from the synthetic bathymetry is quite poor, particularly for the variable T_e synthetic profiles. This explains our decision to invert

gravity data only, rather than inverting bathymetry or performing a joint inversion of gravity and bathymetry.

Also shown in the figure are the effects of profile length on the recovered T_e . We found that a profile length of 250 km recovers T_e poorly, particularly for higher T_e . This is because short profiles omit much of the flexural signal, particularly for stronger lithosphere where the diagnostic wavelength of flexure can exceed 500 km . For input plates with spatial variations in T_e , this means that the inversion fits the weakened section landward of the outer rise without having to fit the strong section seaward of it. The figure shows that inversion of 500 km profiles recovers T_e well for low T_e , but inversion of 750 km profiles provides better recovery for the highest T_e . Inversion of 1000 km long profiles provides no significant improvement.

Fig. 5 shows that when inverting 750 km gravity profiles, the agreement between the input T_e and recovered T_e is very good. This suggests that T_e recovery is little affected by the failure of the broken elastic plate model to account for the gravity effect of low-density sediments in the landward wall of the trench.

6 UNIFORM T_e : INVERSION A1

We begin the inversion using an elastic plate of uniform T_e . Following the results in Fig. 5, 750-km -long ensemble-averaged profiles of free-air gravity anomalies were inverted. Values assumed for densities, elastic parameters and the gravitational acceleration are given in Table 1.

Fig. 6 shows results of segment- and trench-bin profile inversions for each circum-Pacific subduction zone along with the corresponding bending moment and curvature profiles for the best fit T_e . Also shown is the rms difference between observed and calculated

Table 1. The densities and gravitational, elastic and thermal constants assumed in this study. The thermal constants are from the cooling plate model of Parsons & Sclater (1977).

Symbol	Description	Value
g	Acceleration due to Earth's gravity	9.81 m s^{-2}
G	Gravitational constant	$6.67 \times 10^{-11} \text{ m}^3 \text{ kg}^{-1} \text{ s}^{-2}$
E	Young's modulus	100 GPa
ν	Poisson's ratio	0.25
ρ_w	Seawater density	1030 kg m^{-3}
ρ_s	Sediment density	2400 kg m^{-3}
ρ_c	Oceanic crust density	2900 kg m^{-3}
ρ_m	Mantle density	3330 kg m^{-3}
T_t	Thermal lithosphere thickness	125 km
M_t	Temperature at base of thermal lithosphere	1350°C
α	Thermal diffusivity of the lithosphere	$8 \times 10^{-7} \text{ m s}^{-2}$

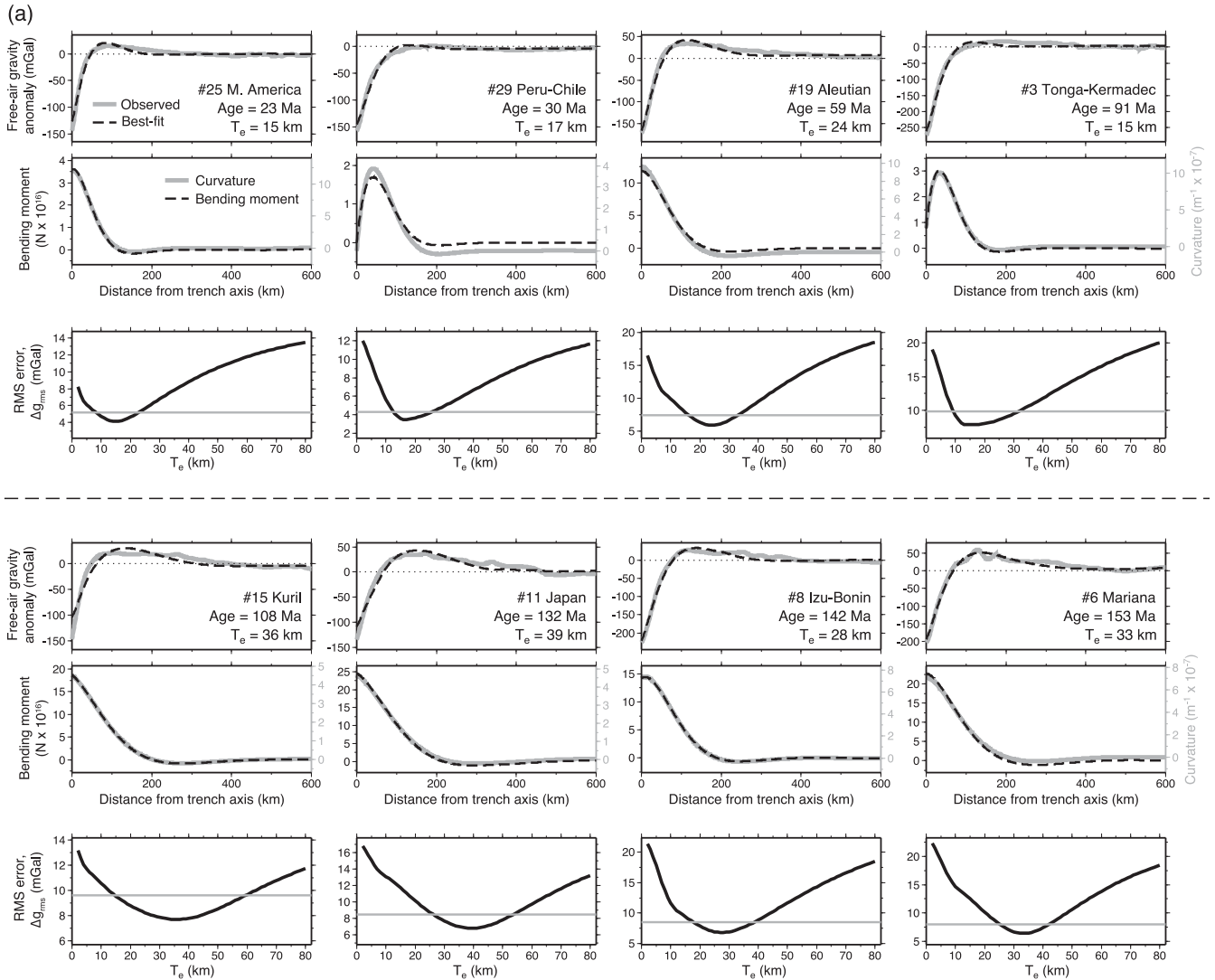


Figure 6. Segment-bin and trench-bin profile fits from Inversion A1, in which a uniform T_e plate was fitted to circum-Pacific trench-outer rise gravity anomalies. For each bin, the top plot shows the observed and best-fitting free-air gravity profile; the trench, average seafloor age and best-fitting T_e are labelled. Beneath each gravity anomaly plot is the corresponding best-fitting bending moment and plate curvature profile. Beneath that is the corresponding plot of T_e versus Δg_{rms} ; the grey line shows 1.25 times the minimum Δg_{rms} , which was used to estimate the uncertainty in T_e . For clarity, only the first 600 km of the profile fits are shown, but the inversions were conducted on 750 km profiles. (a) Segment-bins. Numbers before the trench name refer to the bins, which are numbered in a clockwise direction (Fig. 1). (b) Trench-bins.

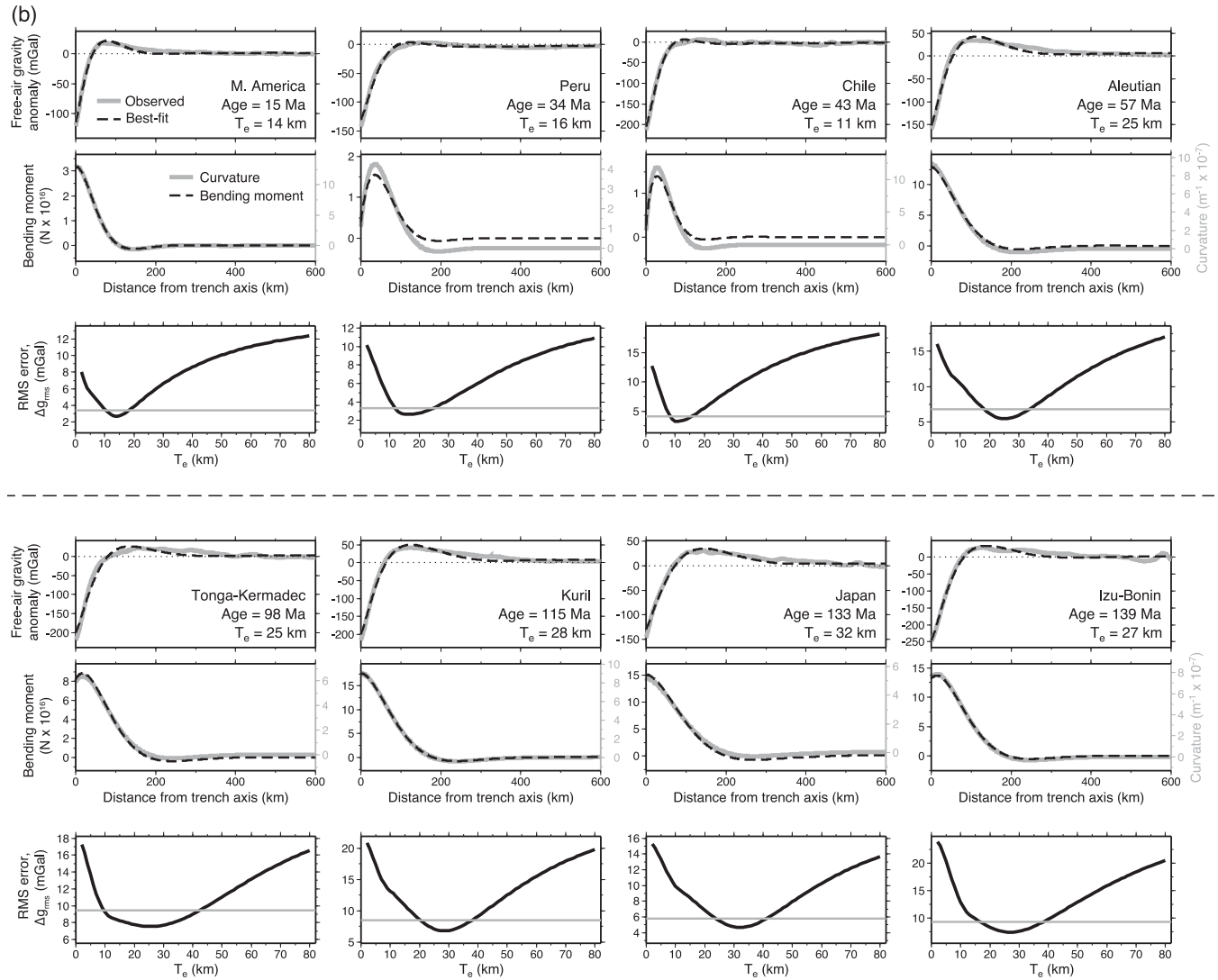


Figure 6. (Continued.)

free-air gravity anomalies, Δg_{rms} , for a range of T_e . Errors in T_e were estimated using 1.25 times the Δg_{rms} minimum (Bry & White 2007). The figure shows that while the rms differences are characterized by a well-defined minimum, a constant T_e plate cannot always simultaneously fit the amplitude and wavelength of the outer gravity high and the steepness of the outer trench-slope (Fig. 4), as is illustrated for the Middle America, Tonga-Kermadec and Kuril segment- and trench-bins. The figure also shows that T_e is well constrained for younger lithosphere, but less so for older lithosphere. This corroborates our synthetic test results, which show that recovered T_e errors are higher for stronger plates.

Fig. 7 shows a plot of the T_e recovered from inversion against the age of the subducting oceanic lithosphere. The figure shows that irrespective of whether segment-bins or trench-bins are used, there is a general increase in the best fit T_e with age. For example, for segment-bins, the Middle America trench (subducting plate age of 2–27 Ma) has a mean T_e of 13.7 ± 1.4 km, Peru–Chile (27–53 Ma) 15.1 ± 4.0 km, Aleutian (52–66 Ma) 25.0 ± 2.4 km, Tonga-Kermadec (85–118 Ma) 26.8 ± 9.0 km, Kuril–Japan (102–136 Ma) 30.7 ± 5.2 km and Izu-Bonin–Mariana (132–57 Ma) 29.5 ± 1.5 km. However, we note that for lithosphere older than ~ 80 Ma, there is no clear increase in T_e with age.

We would expect, based on data from experimental rock mechanics, a dependence of T_e on age and, hence, thermal structure of oceanic lithosphere. This is because ductile creep of lithospheric minerals, such as olivine, is strongly temperature-dependent (e.g. Goetze 1978). Weighted least squares regression, where T_e errors are used as weights, reveals that the relationship between T_e and age is well described by the depth to the $400 \pm 35^\circ\text{C}$ and $380 \pm 57^\circ\text{C}$ isotherms for segment-bins and trench-bins, respectively. The similarity of these isotherms shows results are robust across different bin widths. *Note:* we are not suggesting that these isotherms represent the depth to any physical or petrological boundary; they simply provide a measure of how T_e , which is a proxy for the strength of oceanic lithosphere, varies with age.

Fig. 7 shows that for segment-bins, there is some scatter in the gravity-derived T_e values, particularly for old (> 80 Ma) oceanic lithosphere. However, the figure also shows that T_e is much less scattered for trench-bin profiles, which were ensemble averaged over a larger area and are therefore relatively noise-free. This suggests that at least some of the segment-bin scatter is due to noise in the flexural signal.

We did not invert just for T_e , but also for the end-conditioning forces M_0 and V_0 . To explore the possible trade-offs between T_e

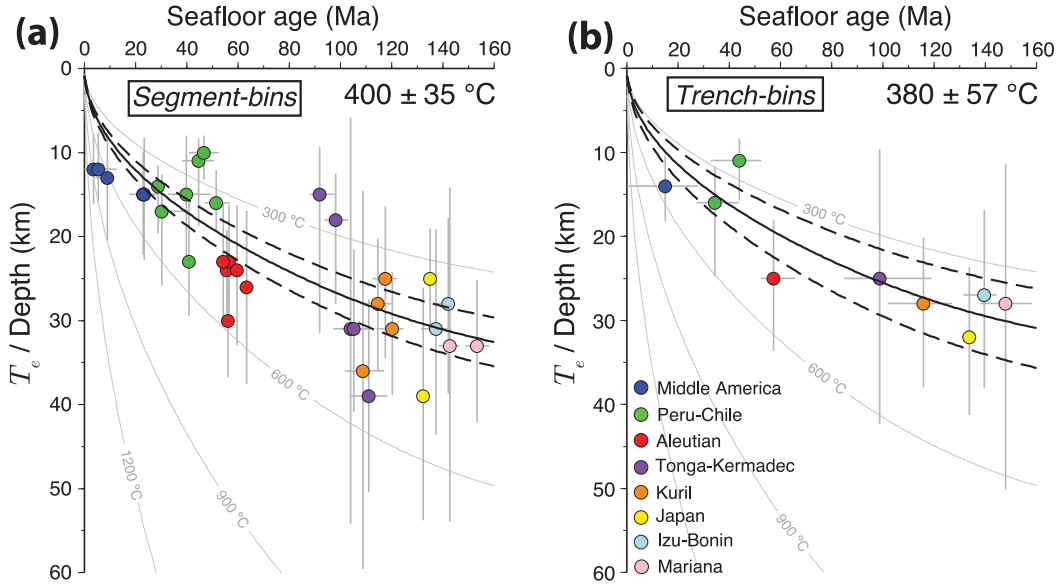


Figure 7. T_e from Inversion A1 plotted against seafloor age for the (a) segment-bins and (b) trench-bins. The uncertainties in T_e and age are shown as straight grey lines. The grey curves show the depth to the plate-cooling isotherms of Parsons & Sclater (1977). The isotherms that best fit the T_e -age relationship are shown in solid black and the 95 per cent confidence intervals in dashed black; the temperatures of these isotherms are labelled in the top right of each plot.

and M_0 and V_0 , a grid search was performed in which M_0 and V_0 were iterated, and at each iteration, T_e was optimized using damped least squares. M_0 was iterated from $(M_0^{\text{best}} - 2M_0^{\text{dev}})$ to $(M_0^{\text{best}} + 2M_0^{\text{dev}})$, where M_0^{best} is the best-fitting value from Inversion A1 and M_0^{dev} is the maximum deviation from M_0^{best} within error (i.e. $\Delta g_{\text{rms}} < 1.25\Delta g_{\text{rms}}^{\text{min}}$). V_0 was iterated from $(V_0^{\text{best}} - 2V_0^{\text{dev}})$ to $(V_0^{\text{best}} + 2V_0^{\text{dev}})$, where V_0^{best} and V_0^{dev} are as described for M_0 .

Fig. 8 shows that there is a trade-off between T_e and M_0 , where T_e increases with the magnitude of M_0 . This is to be expected since in order to produce a given curvature, a larger T_e is required for a larger moment. However, although the trade-off is strong, Δg_{rms} increases rapidly away from the best-fitting value in the M_0 direction and therefore T_e is quite well constrained in this direction. In the V_0 direction, Δg_{rms} increases less rapidly away from the best-fitting value. However, the trade-off between T_e and V_0 is not as strong and therefore T_e is also well constrained in this direction. Furthermore, Fig. 8 suggests that Inversion A1 has found a global, rather than a local, minimum in the ‘hyperspace’ of the T_e objective function.

To examine the robustness of the T_e and plate age relationship, a further series of inversions were conducted to test the sensitivity of the results to: profile length; the degree and order of the long wavelength free-air gravity anomaly that was removed prior to inversion; the constraint on M_0 ; the physical properties of the flexed plate (i.e. Young’s modulus, Poisson’s ratio and density). The main result is that we find the relationship between T_e and age, illustrated in Fig. 7, is robust and does not depend on the assumed physical properties of the plate, the constraint placed on M_0 , or the degree and order of the long wavelength gravity anomaly that has been removed. It is sensitive to profile length, such that the relationship between T_e and age is not clear for short profiles, but synthetic tests show that this is because short profiles omit much of the outer rise, causing T_e to be underestimated for strong lithosphere.

7 VARIABLE T_e : INVERSION A2

As we pointed out earlier, a constant T_e plate is unable to explain all the details of the ensemble averaged free-air gravity anomaly

profiles, as it cannot always simultaneously fit the amplitude and wavelength of the outer gravity high and the steepness of the outer trench-slope. This observation, together with considerations of outer rise faulting and seismicity, suggests that subducting oceanic lithosphere may be weakened as it approaches the trench axis (Contreras-Reyes & Osses 2010; Manríquez *et al.* 2014; Zhang *et al.* 2014; García *et al.* 2015). We therefore carried out a second set of inversions in which the subducting oceanic plate was allowed to weaken in the slope region, landward of the outer rise.

The first step was to define where, and over what distance, the weakening occurs. Contreras-Reyes & Osses (2010) and Manríquez *et al.* (2014) modelled flexure seaward of the Peru-Chile trench using a 2-D and 3-D elastic plate, respectively. They modelled the weakening by arbitrarily defining 3 or 4 constant T_e segments landward of the outer rise crest, using forward modelling and a Monte Carlo optimization technique, respectively to find the best-fitting T_e for each segment. Zhang *et al.* (2014) modelled flexure at the Mariana trench using an elastic plate with two constant T_e segments, where the width of the segments was found using an inverse approach. The approach of Contreras-Reyes & Osses (2010) and Manríquez *et al.* (2014) entails defining the outer rise crest, which is often difficult to do in the presence of seamounts or other short wavelength bathymetric features or in regions without a pronounced outer rise. The method of Zhang *et al.* (2014), on the other hand, adds another free parameter to the inversion, which introduces additional trade-offs and reduces resolution of inverted parameters such as T_e .

In light of these considerations, we chose to use the plate curvature to define where weakening occurs, as this is likely to exert a first order control on the long-term strength evolution of the subducting plate through bending-induced inelastic yielding (e.g. McNutt & Menard 1982).

The curvature, κ , cannot, however, easily be calculated from observed bathymetry, as it is very sensitive to small fluctuations in seafloor depth. Therefore, for each bin, a constant T_e elastic plate was fitted to 170 km long ensemble-averaged free-air gravity anomaly profiles, using the same procedure as in Inversion A1, and the curvature calculated from the best-fitting model profile. The relatively short profile length allows the inversion to fit the

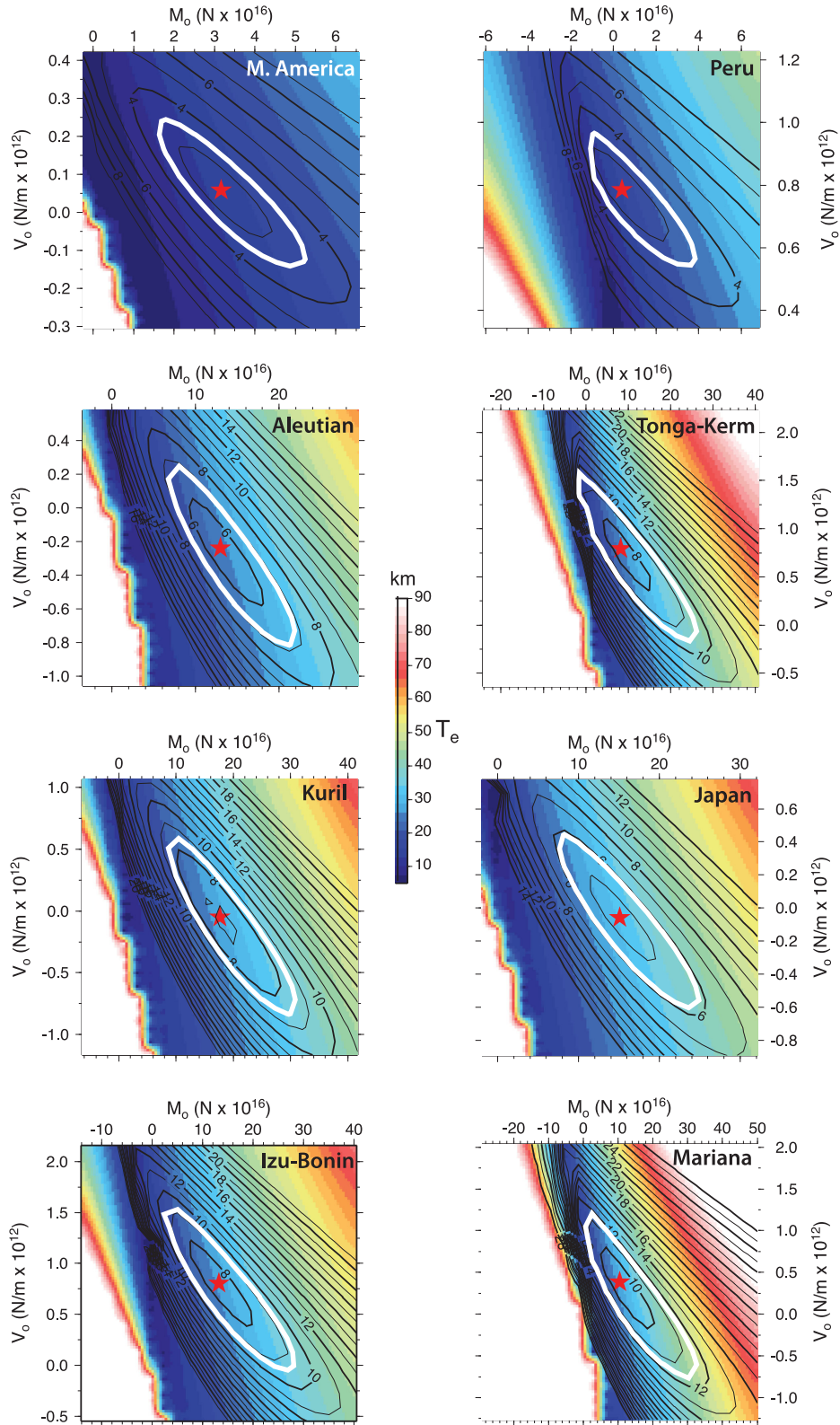


Figure 8. Plots showing the trade-offs between M_0 , V_0 and T_e for the trench-bin profiles; the trench is labelled on the top right of each plot. To calculate this, M_0 and V_0 were iterated and T_e optimized at each iteration using a damped least squares algorithm. The colour map shows the best-fitting T_e . The RMSE between the observed and calculated gravity, Δg_{rms} , is contoured every 1 mGal up to a maximum of three times the minimum Δg_{rms} . The white contour is 1.25 times the minimum Δg_{rms} , which was used to estimate the T_e uncertainty in Inversion A1. The red star shows the best-fitting solution from Inversion A1.

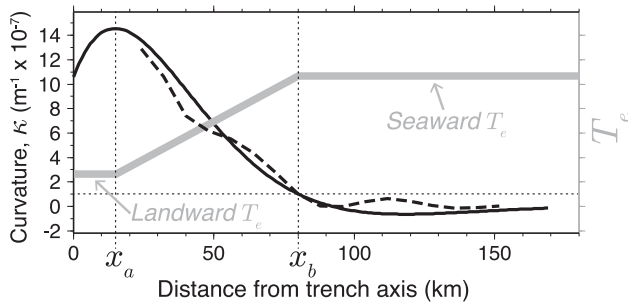


Figure 9. Figure showing how the observed curvature (solid black) was used to define the location of plate weakening (grey) in Inversion A2. The ‘observed curvature’ was estimated by fitting an elastic plate to 170-km-long gravity profiles, and was verified by comparison to the curvature estimated from bathymetry using a moving window regression (dashed black).

steepness and curvature of the outer trench-slope without having to fit all the features of the outer rise.

To determine whether this approach reproduces the actual curvature, we directly estimated the curvature of the trench-bin ensemble-averaged bathymetry profiles, which are relatively smooth (compared to the segment bin profiles) owing to the large area over which they are averaged. To do this, $\frac{dw}{dx}$ was estimated using a linear regression in a 40-km-wide moving-window. This was then median filtered with a 10 km filter width and differentiated to give κ .

As illustrated in Fig. 9, the curvature estimates from the two methods show good agreement, suggesting that the 170 km elastic plate provides a reliable estimate of the actual curvature of the lithosphere. From here on, the term ‘observed curvature’ will refer to the curvature estimated by the elastic-plate fitting method described above.

After the observed curvature was derived, the next step was to use it to define where, and over what distance, the plate weakening occurs. Whilst previous authors allowed abrupt spatial changes in T_e (Contreras-Reyes & Osses 2010; Manriquez *et al.* 2014; Zhang *et al.* 2014), we chose to let it decrease linearly from a T_e seaward of the outer rise (‘seaward T_e ’, Fig. 9) to a T_e landward of the outer rise (‘landward T_e ’, Fig. 9). Our reasoning for this is that when observed curvatures are applied to experimentally derived YSEs, an approximately linear reduction in rigidity is predicted as the lithosphere approaches the trench. As Fig. 9 shows, T_e is allowed to decrease landward of the point x_b , at which $\kappa = 1 \times 10^{-7} \text{ m}^{-1}$. This threshold curvature is arbitrarily chosen so that it is far enough landward to constrain the seaward T_e value, but far enough seaward to fit the gravity anomaly profile well. In reality, T_e will begin to decrease as soon as the plate starts to bend (i.e. $\kappa > 0$), but if weakening were allowed landward of this point, there would be little or no deflection in the free-air gravity anomaly with which to fit the seaward T_e value.

We stipulate that the linear landward decrease in T_e terminates at the point of maximum curvature, x_a (Fig. 9). This point generally occurs close to the trench axis: the mean distance from the axis is 23 ± 10 km and the range is 0–42 km. Landward of x_a , the decrease in observed curvature suggests that the subducting plate may begin to unbend, which cannot be modelled by a static elastic plate (e.g. Turcotte *et al.* 1978; Bodine & Watts 1979; Mueller *et al.* 1996). However, the decrease in curvature might instead reflect sedimentary processes, for example, turbidite deposition in the trench, or free-air gravity anomalies caused by the landward wall of the trench or shallow geological structures in the forearc crust.

Our variable T_e inversion method is as follows. First, landward T_e was iterated from 2 to 60 km in steps of 1 km and at each iteration, four parameters were optimized using damped least squares: seaward T_e , M_o , V_o and c . Then, to estimate errors on seaward T_e , landward T_e was held fixed at its best-fitting value and seaward values were iterated upward of this to 100 km; at each iteration, three parameters were optimized: M_o , V_o and c . We chose to iterate over landward T_e first because this is better constrained than seaward T_e due to the relatively high signal-to-noise ratio (SNR) close to the trench axis. We note that this inversion method does not force the plate to weaken: it is possible for best-fitting values of landward and seaward T_e to be equal.

Fig. 10 shows the results of the variable T_e inversion for the trench-bin profiles for each circum-Pacific subduction zone, along with the corresponding T_e , bending moment and curvature. Relative to the uniform T_e inversion case, A1 (Fig. 6), Δg_{rms} is improved by an average of 39 per cent and by up to 73 per cent, which is quite substantial given that the calculated anomalies seaward of the outer rise are changed little. The plate weakens in 42 out of 43 best-fitting models, where the average reduction in T_e is 51 ± 11 per cent and the range is 20–72 per cent with most values in the range 40–65 per cent.

Fig. 11 shows that, as in the case of uniform T_e (Fig. 7), there is a clear increase in both landward and seaward T_e with age of the subducting oceanic lithosphere. For example, for segment-bins, the Middle America trench (2–27 Ma) has a mean landward T_e of 12.0 ± 1.2 km, Peru–Chile (27–53 Ma) 13.7 ± 2.7 km, Aleutian (52–66 Ma) 20.8 ± 2.3 km, Tonga–Kermadec (85–118 Ma) 22.8 ± 3.5 km, Kuril–Japan (102–136 Ma) 23.7 ± 2.3 km, and Izu–Bonin–Mariana (132–157 Ma) 27.5 ± 3.2 km. Trench-bin and segment-bin estimates are well fit by the $342 \pm 35^\circ\text{C}$ and $349 \pm 22^\circ\text{C}$ cooling plate model isotherms, respectively, once again showing that our results are robust across different bin widths.

We find that landward T_e is better constrained and less scattered than seaward T_e (Fig. 11). This is because the SNR is significantly higher closer to the trench axis and because the flexural wavelength is more sensitive to lower than higher T_e . However, it is clear that irrespective of the binning (segment or trench) there is a general increase in seaward T_e with age. For example, for segment-bins, the Middle America trench (2–27 Ma) has a mean seaward T_e of 25.8 ± 9.8 km, Peru–Chile (27–53 Ma) 26.8 ± 7.4 km, Aleutian (52–66 Ma) 42.8 ± 6.8 km, Tonga–Kermadec (85–118 Ma) 52.3 ± 6.5 km, Kuril–Japan (102–136 Ma) 52.2 ± 13.5 km and Izu–Bonin–Mariana (132–157 Ma) 48.6 ± 5.8 km. Trench-bin and segment-bin estimates are best fit by the $714 \pm 75^\circ\text{C}$ and $671 \pm 59^\circ\text{C}$ oceanic isotherms, respectively.

The relationship between landward T_e and age is less scattered than in Inversion A1. This suggests that some of the scatter in Inversion A1 results from modelling the lithosphere with a plate of uniform T_e and/or the relatively low SNR seaward of the outer trench-slope.

The best-fitting isotherms to seaward and landward T_e from Inversion B1 are higher and lower, respectively than that obtained in Inversion A1. This is expected, as the uniform T_e estimates from Inversion A1 reflect an average of the subducting oceanic lithosphere’s decreasing strength as it moves up and over the outer rise and descends into the trench. Seaward T_e , however, reflects an average of only the relatively strong region seaward of the outer rise, whilst landward T_e reflects only the relatively weak region landward of this. Landward T_e is an average of 3.5 km lower than the T_e from Inversion A1, whilst seaward T_e is an average of 18.1 km higher. This shows that the uniform T_e estimates from Inversion A1 are

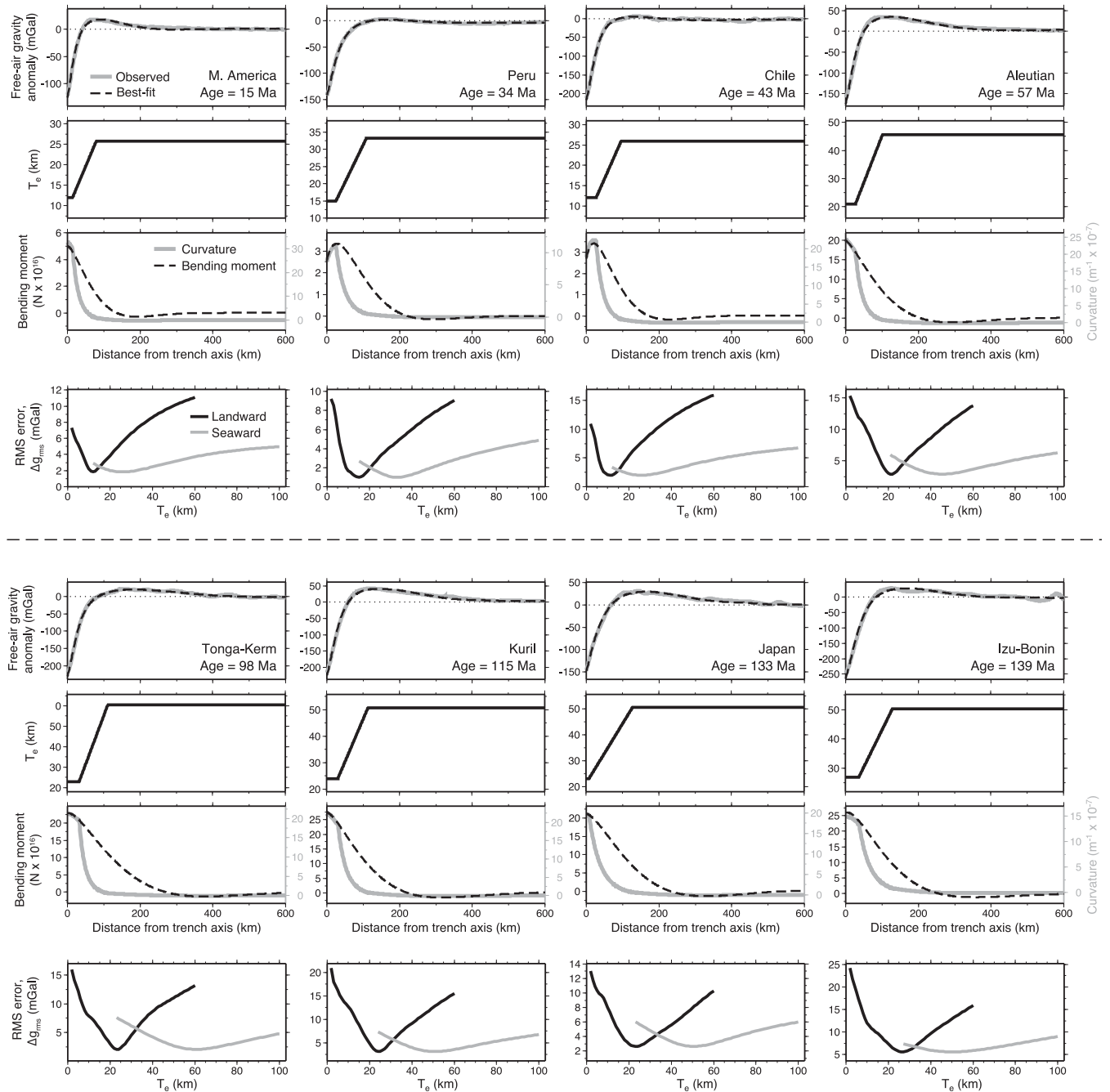


Figure 10. Trench-bin profile fits from Inversion A2, in which a variable T_e plate model was fit to circum-Pacific trench-outer rise free-air gravity anomalies. For each bin, the top plot shows the observed and best-fitting gravity profile; the trench and average seafloor age are labelled. Note that these are the same bins as shown in Fig. 6(b). Beneath each gravity anomaly plot is the corresponding best-fitting T_e profile, and beneath that, the corresponding bending moment and curvature profile. Beneath that is the corresponding plot of landward T_e (black line) and seaward T_e (grey line) versus Δg_{rms} . For clarity, only the first 600 km of the profile fits are shown, but the inversions were conducted on 750 km profiles.

biased towards the low strength close to the trench axis, which is in accord with results from the inversion of synthetic profiles.

We have tested the sensitivity of results to the assumed position of plate weakening, which shows that the modelled seaward T_e is somewhat sensitive to the position of x_b (Fig. 9). For example, if x_b is defined as the point at which $\kappa = 2 \times 10^{-7} \text{ m}^{-1}$, rather than $\kappa = 1 \times 10^{-7} \text{ m}^{-1}$, seaward T_e is decreased by a mean of 2.2 km, and if x_b is defined as the point at which $\kappa = 0$, seaward T_e is increased by a mean of 3.5 km. However, the change in seaward

T_e with x_b is age-invariant and therefore does not affect the result that there is a clear increase in T_e with age. The sensitivity of seaward T_e to x_b is not surprising, as the further landward x_b is, the more flexurally weakened lithosphere is modelled by the seaward T_e . Tests also show that the modelled landward T_e is insensitive to the position of x_b , and only moderately sensitive to the position of x_a . For example, if x_a is shifted 10 km landward, landward T_e is decreased by a mean of 1.3 km, and if x_a is shifted 10 km seaward, landward T_e is increased by a mean of 1.5 km.

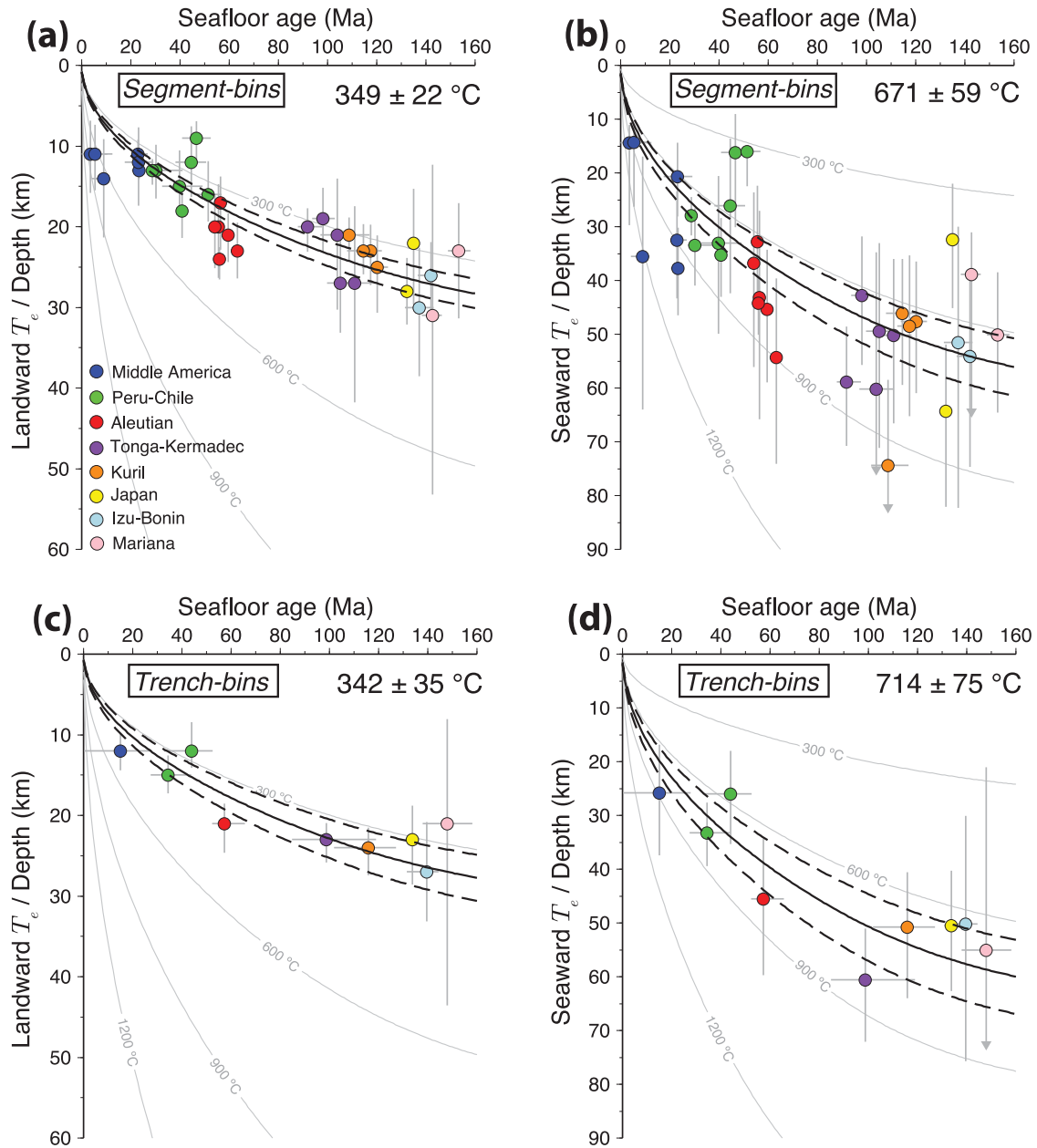


Figure 11. T_e from Inversion A2 plotted against seafloor age for the (a, b) segment-bins and (c, d) trench-bins. (a, c) shows the landward T_e and (b, d) shows the seaward T_e . The uncertainties in T_e and age are shown as straight grey lines; arrows on error bars indicate an unconstrained upper bound on T_e . The grey curves show the depth to the plate-cooling isotherms of Parsons & Sclater (1977). The isotherms that best fit the T_e -age relationship are shown in solid black and the 95 per cent confidence intervals in dashed black; the temperatures of these isotherms are labelled in the top right of each plot.

Inversion A2 shows that the fit to almost all of the observed free-air gravity profiles is improved by a plate that weakens landward of the outer rise, where the average reduction in T_e between seaward and landward values is 51 ± 11 per cent and the maximum is 72 per cent. This suggests that plate weakening is a ubiquitous feature of the trench-outer rise of circum-Pacific subduction zones, and corroborates previous studies suggesting plate weakening at the Mariana (Bodine & Watts 1979; Zhang *et al.* 2014), Bonin (Bodine *et al.* 1981), Chile (Contreras-Reyes & Osses 2010; Manriquez *et al.* 2014), Kermadec (Billen & Gurnis 2005) and Aleutian, Kuril and Tonga trenches (Turcotte *et al.* 1978). Inversion A2 also shows that the percentage plate weakening is similar for different trenches and does not vary with plate age.

Plate weakening at the trench-outer rise region is most likely caused by bending-induced inelastic yielding (e.g. Goetze & Evans 1979; Bodine *et al.* 1981), where flexural stresses cause the lithosphere to yield through shallow, brittle processes such as faulting and deep, ductile processes such as dislocation creep. There is abundant observational evidence of shallow brittle failure at the outer trench-slope of subduction zones. Swath bathymetry (e.g. Jones *et al.* 1978; Masson 1991; Grevemeyer *et al.* 2005) and seismic imaging (Ranero *et al.* 2003) reveals that the majority of outer trench-slopes are pervasively fractured by extensional bend-faults (Appendix A). Bend-faulting is also reflected in seismicity at the outer trench-slope (e.g. Chappelle & Forsyth 1979; Christensen & Ruff 1988; Craig *et al.* 2014). These events are predominantly

tensional and occur at shallow depths (<30 km); deeper compressional earthquakes occur less frequently and are separated from shallow events by an aseismic core, which reflects the region where stresses are not high enough to cause yielding.

Bend-faults may further contribute to lithospheric weakening by providing a pathway for seawater to enter and subsequently alter the crust and uppermost mantle. Hydration of the uppermost mantle at the outer trench-slope is evidenced by anomalously low P -wave velocity (e.g. Ranero & Sallares 2004; Grevemeyer *et al.* 2007; Contreras-Reyes *et al.* 2008a), heat flow (Yamano & Uyeda 1990; Grevemeyer *et al.* 2005) and seismic anisotropy, and anomalously high Poisson's ratio (Contreras-Reyes *et al.* 2008b).

Hydration of mantle peridotite at temperatures <400–500 °C results in serpentinization of olivine. This may further weaken the lithosphere in the brittle regime, as laboratory experiments show that serpentine has lower friction (Dengo & Logan 1981; Moore *et al.* 1997) and fracture (Raleigh & Paterson 1965; Escartin *et al.* 1997) strength than most lithospheric rocks. Experiments on peridotite cores with 10–15 per cent serpentine show that the brittle strength is comparable to that of pure serpentinite (Escartin *et al.* 2001). P -wave velocities from active-source seismic studies suggest up to 20–25 per cent serpentinization of the uppermost mantle beneath the outer trench-slope (Ranero & Sallares 2004; Grevemeyer *et al.* 2007; Contreras-Reyes *et al.* 2008a), and thus significant brittle weakening may occur. Laboratory studies show that serpentine is also weaker than olivine in the dislocation creep regime, and thus the lithosphere may be further weakened in the ductile regime if bend-faults facilitate hydration to great enough depth.

8 DISCUSSION

We have shown (e.g. Figs 7 and 11) that there is a first-order increase in the elastic thickness, T_e , with oceanic plate age at circum-Pacific trench systems. This result is independent of analysis bin size and whether or not a uniform or variable T_e elastic plate (flexure) model is used. This finding is generally consistent with previous studies of volcano loading at seamounts and oceanic islands in the plate interiors which show that T_e is given approximately by the depth to the 300–600 °C oceanic isotherms based on a cooling plate model. In this section, we examine the robustness of the relationship between T_e and oceanic plate age seaward of circum-Pacific trenches and then explore its potential for discriminating between different laboratory-derived flow laws for oceanic mantle-type rocks.

8.1 Scatter in T_e versus age plots

Irrespective of the role of plate weakening, there is some scatter in our plots of T_e against plate age. This suggests that there might be other factors that affect the rigidity of oceanic lithosphere as it approaches a trench. For example, the lithosphere may be permanently weakened by hotspot-induced thermal rejuvenation (e.g. McNutt 1984; Smith *et al.* 1989) such that the plate is unable to recover its strength with time. This could affect T_e in regions where the subducting plate has been influenced by hotspot volcanism, for example, at the Mariana (Marcus-Wake guyots), Tonga-Kermadec (Louisville Ridge, Mannihiki Plateau) and Peru-Chile (Nacza Ridge) trenches. Also, T_e at the trench-outer rise may be affected by variation in the axial force acting on the subducting plate, as laboratory-derived YSEs predict that even relatively small levels of axial normal stress (>100 MPa) can have a significant effect on the effective flexural rigidity of oceanic lithosphere (McNutt 1984; Mueller *et al.* 1996;

Garcia-Castellanos *et al.* 2000). The axial force should vary between and along trenches depending on the balance between the tectonic driving forces such as slab pull and ridge push (Forsyth & Uyeda 1975; Richardson 1992) and so we would expect to see some variation in T_e along-strike deep-sea trench-outer rise systems.

The accuracy of our T_e estimates will also be affected by short-wavelength bathymetric features such as seamounts, fracture zone ridges and troughs, and abyssal hill fabric, which may be superimposed on the outer rise. In addition, T_e might vary in regions where the assumptions in the elastic plate model of cylindrical bending model break down. For example, Wessel (1996) showed that cylindrical modelling might introduce up to 30 per cent bias in T_e estimates in regions of arcuate trench geometry, such as the Arica Bight at the Peru–Chile trench. As the loads acting on the subducting plate are unknown, we inverted for an applied moment and shear force at the trench axis. Any inaccuracies therefore in the recovered end-loads may also contribute to inaccuracies in T_e .

The T_e recovered from free-air gravity anomalies might also be affected by local gravity anomalies that are not directly caused by trench-outer rise flexure. Our synthetic modelling included the gravity effect of low-density sediments in the forearc, and results show that this has little effect on the recovered T_e . However, the synthetic model did not account for any gravity anomalies that may result from hydration of the uppermost mantle through bend faulting on the outer trench-slope.

The reduction in P -wave velocity that has been observed beneath the outer trench-slope suggests up to 20–25 per cent serpentinization of the uppermost mantle (Ranero & Sallares 2004; Grevemeyer *et al.* 2007; Ivandic *et al.* 2008; Contreras-Reyes *et al.* 2008a), which corresponds to a reduction in density of 150–200 kg m^{−3} (Escartin *et al.* 2001). This should result, depending on the geometry of the hydrated region, in a localized negative gravity anomaly that increases the magnitude of the gravity anomaly ‘low’ that is observed at the outer trench-slope. The model used in this study does not account for this and we note that this is a potential weakness of the present study. However, as bend-faulting appears to have been observed at both young (Ranero & Sallares 2004; Grevemeyer *et al.* 2007) and old (Contreras-Reyes *et al.* 2011; Stratford *et al.* 2015) trenches, we do not believe that hydration of the uppermost mantle will significantly affect our conclusion that T_e increases with the age of the subducting plate, either within the region of plate weakening or seaward of it.

Figs 7 and 11 show that there is no clear increase in T_e with plate age for lithosphere older than 80 Ma. We suggest two main reasons for this. First, the rate of oceanic plate cooling slows with age, and is particularly slow for lithosphere older than ~70 Ma as the thermal structure begins to ‘feel’ the influence of the lower thermal boundary layer (Parsons & Sclater 1977). This means that for older lithosphere, the thermal structure and therefore ductile flow strength will change little with plate age. For example, the depth to the 600 °C plate-cooling isotherm increases by only 11 km from 80 to 150 Ma, compared to an increase of 24 km from 10 to 80 Ma.

Second, the flexural parameter, α , which reflects the wavelength of flexure, is proportional to $T_e^{3/4}$ (Watts 2001):

$$\alpha = \left[\frac{4-D}{(\rho_m - \rho_w)g} \right]^{1/4}. \quad (8)$$

This means that the sensitivity of the flexural wavelength to T_e decreases with increasing rigidity. As a result, changes in T_e are more difficult to detect for older, stronger lithosphere, particularly in the presence of short-wavelength noise such as seamounts, and

thus T_e estimates are more uncertain. This is reflected in the results from inversion of synthetic profiles (Fig. 5), which show that T_e is less well constrained for stronger input plates than for weaker input plates.

8.2 Comparison with Bry & White (2007)

The results from Inversions A1 and B1 that T_e increases with age of the subducting oceanic lithosphere contrasts strikingly with those of Bry & White (2007), who used a similar overall approach to that used here. They found, using 700-km-long profiles of gravity or bathymetry, no clear relationship between T_e and plate age, suggesting that either oceanic lithosphere does not strengthen with age or that T_e is a parameter that is insensitive to the integrated strength of the lithosphere (Fig. 12a). There are differences, however, in the analysis between the two studies and so we have carried out two further inversions (C1 and C2) in an attempt to resolve the cause of these differences. As well as inverting the observed ensemble-averaged free-air gravity profiles, we also inverted the suite of variable-rigidity synthetic profiles that were described earlier, so that we could further test the efficacy of these inversions. We compare our results to the gravity-derived results of Bry & White (2007), but note that they conducted a separate inversion of bathymetry, which yielded similar results.

Two differences between this study and that of Bry & White (2007) are explicitly clear. First, to account for any long-wavelength free-air gravity anomalies unrelated to trench-outer rise flexure, we removed a spherical harmonic expansion of Earth's gravity field (EGM2008, Pavlis *et al.* 2012) up to degree and order 16 prior to inversion. In contrast, Bry & White (2007) inverted for a linear gravity anomaly slope. Second, in this study, elastic plate deflections were calculated using an exact line integral method (Bott 1960) taking into account the actual density contrasts at the seafloor, top crust and Moho interfaces. In contrast, Bry & White (2007) appear to have used a simple Bouguer slab approximation that accounts for only a single density contrast and so fails to take into account the contribution to the gravity anomaly of all the flexed surfaces (see, for example, eq. 10 of Bry & White 2007 and their comment that they 'do not include all possible density contrasts').

Inversion C1 was used to test the effect of these differences on T_e recovery. In this inversion, a linear slope in the free-air gravity anomaly was optimized for and the calculated flexure was converted to gravity using a single interface and the Bouguer slab approximation. Fig. 12(b) shows that this approach generally yields a lower circum-Pacific T_e than Inversion A1, with a mean reduction of 3.3 km, and that the largest reduction occurs for older lithosphere, with a mean of 4.8 km. As a result, the relationship between T_e and plate age is significantly 'flattened' relative to Inversion A1. These results are in accord with synthetic modelling (Fig. 12c), which show that Inversion C1 generally underestimates the input T_e and that the underestimation is greater for stronger than weaker input plates.

In addition to the differences described above, the observed and modelled gravity anomaly profiles presented by Bry & White (2007) suggest two other differences with this study. First, a number of the observed bathymetry and free-air gravity anomaly profiles used by Bry & White (2007) display negative curvature, that is are concave upwards, at the plate-break of their model. It is not immediately clear to us why this is. One possibility is that the trench axis was inaccurately located and was placed landward of the actual bathymetrically defined axis, where the upward deflection of the landward

trench wall causes an upward deflection in the gravity anomaly. In contrast, in this study, the trench axis was located using an automated algorithm that traces the along-trench bathymetric minimum (Bassett & Watts 2015). Second, in this study, the bending moment applied at the trench axis, M_0 , was constrained to be positive. In contrast, it appears that Bry & White (2007) did not exert any constraint on M_0 , as some of their best-fitting profiles fit the negative curvatures of their observed profiles at the trench axis.

Inversion C2 was used to test the additional effect of these differences. This was similar to Inversion C1—in that a linear gravity anomaly slope was optimized for and a Bouguer slab approximation was used to calculate the gravity—but with two modifications. First, the plate-break was placed 10 km landward of the bathymetrically defined trench axis and second, no constraint placed on M_0 . Fig. 12(b) shows that Inversion C2 generally yields lower circum-Pacific T_e than Inversions A1 and C1, and that the relationship between T_e and plate age is further flattened. As a result, there is no perceivable increase in T_e with age. These results are in accord with the results of synthetic modelling (Fig. 12c), which show that Inversion C2 generally yields lower T_e than Inversion C1.

The results of Inversions C1 and, in particular, C2 (Fig. 12b) are qualitatively similar to the results of Bry & White (2007; Fig. 12a): there is no clear relationship between T_e and plate age and the upper bounds on T_e are very poorly constrained. Thus, we suggest that the discrepancy between this study and that of Bry & White (2007) can be accounted for by a combination of factors which include: the manner of the long wavelength gravity field removal; the method used to calculate gravity anomalies; the constraint placed on M_0 ; and the location of the trench axis. Of these factors, the long wavelength gravity field is probably the most important, as we have found that it produces the most significant flattening of T_e with plate age.

8.3 Constraining experimentally derived oceanic mantle flow laws

As Goetze & Evans (1979) and Burov & Diament (1995) have previously shown for the oceans and continents, respectively, once the curvature of flexure associated with a load on the plate is known then it is possible to use the yield strength envelope (YSE) derived from experimental rock mechanics data to predict T_e . This predicted T_e can then be compared to the observed T_e in order to constrain lithospheric rheology and test the predictions of laboratory-derived flow laws. We have therefore used the T_e estimates derived here to constrain the rheology of subducting oceanic lithosphere, and in particular the rheology in the low temperature plasticity (LTP) regime, at circum-Pacific subduction zones.

The YSE for oceanic lithosphere is based on two main deformation regimes: a relatively shallow brittle regime and a relatively deep ductile regime. Fig. 13 shows the yield strength in each of these regimes for 80 Ma oceanic lithosphere, a uniform strain rate of 10^{-16} s^{-1} and a range of different ductile flow laws.

In the case that the shallow lithosphere is pervasively fractured then the brittle regime can be described by the Coulomb-Navier failure criterion for frictional sliding on pre-existing fault surfaces (e.g. Goetze & Evans 1979; Kohlstedt *et al.* 1995). This criterion assumes that the brittle yield strength of a fault is given by the sum of its frictional strength and its cohesive strength due to chemical bonding across the fault:

$$\tau = C_o + \mu_f (\sigma_n - P_f), \quad (9)$$

where τ is the shear strength, C_o is the cohesive strength, μ_f is the coefficient of friction, σ_n is the normal stress acting across the fault,

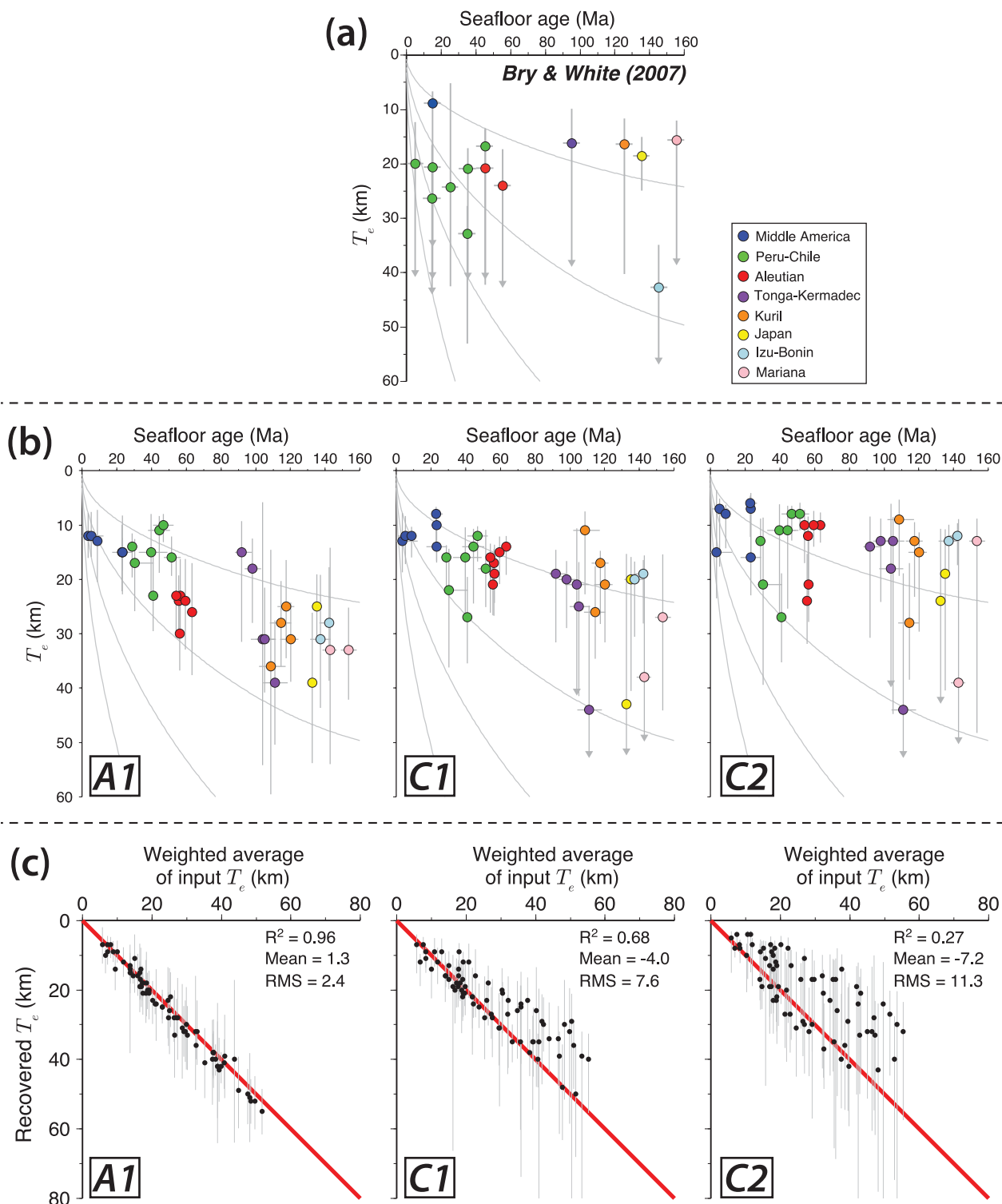


Figure 12. Figure showing the results of Inversion C1 and C2, which were used to understand the discrepancy between our results and those of Bry & White (2007). (a) Circum-Pacific T_e estimates digitized from Bry & White (2007), which were obtained by inversion of 700 km long, averaged profiles of free-air gravity; arrows on error bars indicate an unconstrained upper bound on T_e . (b) Circum-Pacific T_e from our preferred inversion, Inversion A1, compared to Inversions C1 and C2. (c) Results from inversion of a suite of variable-rigidity synthetic profiles. The input T_e is given as a weighted average of the input T_e profile, weighted by the squared magnitude of the input T_e profile.

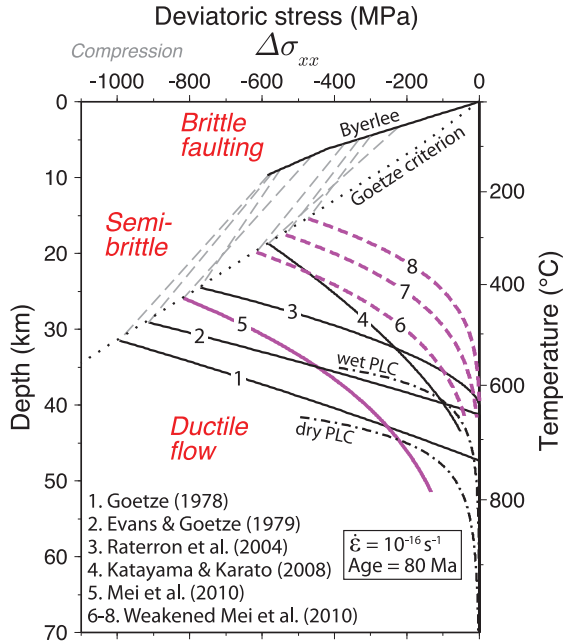


Figure 13. The yield strength predicted by the brittle and ductile failure laws used in this study. The shallow, brittle yield strength was calculated with Byerlee's (1978) friction coefficients and hydrostatic PFP. The yield strengths for the LTP flow laws are numbered 1–8. The solid and dashed purple lines highlight the Mei *et al.* (2010) LTP flow law and the weakened Mei *et al.* (2010) LTP flow laws, respectively. The dotted-dashed lines show the yield strengths for the dry and wet PLC laws of Hirth & Kohlstedt (2003). The semi-brittle regime is marked in dashed grey. The yield strengths were calculated for an 80 Ma plate-cooling geotherm and $\dot{\epsilon} = 10^{-16} \text{ s}^{-1}$.

and P_f is the pore–fluid pressure (PFP). Byerlee (1978) found from experimental data that C_o and μ_f are nearly independent of rock type and temperature:

$$\begin{aligned} \tau &= 0.85(\sigma_n - P_f), \quad \sigma_n \leq 200 \text{ MPa} \\ \tau &= 50 + 0.6(\sigma_n - P_f), \quad \sigma_n > 200 \text{ MPa}. \end{aligned} \quad (10)$$

The ductile regime is often described in terms of the rheological behavior of dry polycrystalline olivine (e.g. Karato *et al.* 1993; Hirth & Kohlstedt 1996). At the relatively low temperatures ($< 1350^\circ\text{C}$) and high deviatoric stresses ($> 10 \text{ MPa}$) typical of lithospheric deformation, laboratory studies suggest that dislocation creep is the dominant deformation mechanism (e.g. Goetze 1978; Kohlstedt *et al.* 1995), and this is supported by observations of seismic anisotropy and of lattice preferred orientation (LPO) in crustal rocks sampled from ductile shear zones (Kohlstedt *et al.* 1995).

For lithospheric conditions, dislocation creep can occur through two main mechanisms. At lower temperatures ($\approx 600\text{--}800^\circ\text{C}$) and higher stress ($\approx 100\text{--}300 \text{ MPa}$), dislocation creep is rate-limited by the glide of dislocations, which is controlled by the intrinsic resistance of the lattice, known as the Peierls stress (e.g. Goetze 1978; Evans & Goetze 1979). This mechanism, which is commonly referred to as low-temperature plasticity (LTP), can be expressed by:

$$\dot{\epsilon} = A\sigma^n \left\{ -\frac{H_0^*}{RT} \left[1 - \left(\frac{\sigma}{\sigma_p} \right)^p \right]^q \right\}, \quad (11)$$

where $\dot{\epsilon}$, σ , T and R are the strain rate, differential stress, temperature, and gas constant, respectively; A is a pre-exponential term that depends on pressure, grain size and volatile content; n is a non-dimensional parameter that arises from the stress-dependence of dislocation density; H_0^* is the zero-stress activation enthalpy; σ_p

is the Peierls stress or glide resistance; p and q are non-dimensional parameters that depend on the geometry of kinks (Kocks 1975; Mei *et al.* 2010).

We test here five different laboratory-derived LTP flow laws (Goetze 1978; Evans & Goetze 1979; Raterron *et al.* 2004; Katayama & Karato 2008; Mei *et al.* 2010, labelled 1–5 in Fig. 13 and defined in Table 2). In addition, a further three flow laws were tested, which are labelled 6–8 in Fig. 13 and listed in Table 2 as $M(10^4)$, $M(10^6)$ and $M(10^8)$. These correspond to weakened cases of the law of Mei *et al.* (2010), where the pre-exponential term, A , has been increased by 4, 6 and 8 orders of magnitude, respectively. We included these cases in light of the study of Zhong & Watts (2013), who used a 3-D finite-element viscoelastic model, together with a laboratory-derived effective viscosity, to compute the flexure beneath the volcanic loads of the Hawaiian Islands in the Central Pacific Ocean. They found that the law of Mei *et al.* (2010) is much too strong to fit the observed, seismically constrained, flexure and that it must be significantly weakened in order to explain the observations.

At higher temperature ($\gtrsim 600\text{--}800^\circ\text{C}$) and lower stress ($\gtrsim 100\text{--}300 \text{ MPa}$), dislocation creep is rate-limited by the climb of dislocations (e.g. Goetze 1978; Chopra & Paterson 1984; Hirth & Kohlstedt 2003). This mechanism is commonly known as power-law creep (PLC) and its constitutive equation is of the form:

$$\dot{\epsilon} = B\sigma^n \exp\left(-\frac{E^* + PV^*}{RT}\right), \quad (12)$$

where B is a material-dependent parameter that can include the influence of water content, n is the stress exponent, E^* is the activation energy, P is pressure, and V^* is the activation volume. We used two published PLC flow laws in this study (dashed-dotted lines in Fig. 13), one for dry olivine and one for wet olivine, and the relevant parameters are given in Table 3.

It is usually assumed that the brittle and ductile flow deformation regimes are independent and that the one with smaller strength dominates (e.g. Goetze & Evans 1979; Kohlstedt *et al.* 1995). However, there is a poorly understood, transitional semi-brittle regime where deformation occurs through a mix of processes (grey dash lines in Fig. 13). Deformation experiments on calcite marble (Edmond & Paterson 1972), halite (Shimamoto 1986) and granite (Stesky 1978) suggest that the shallow portion of the semi-brittle regime is characterized by localized, stable frictional sliding that is accommodated by a mixture of brittle and ductile processes, whilst the deeper portion is characterized by distributed deformation that involves plastic flow and homogeneously distributed microcracks (Kohlstedt *et al.* 1995). The transition between the brittle and semi-brittle regimes occurs when the ductile yield strength is about five times the brittle yield strength, and the transition between the semi-brittle and ductile regimes is defined by the Goetze criterion, which states that brittle processes will contribute to deformation for differential stresses larger than the overburden pressure (Kohlstedt *et al.* 1995). There are, however, no flow laws to adequately describe the semi-brittle regime and so we have not included them in the construction of our YSEs.

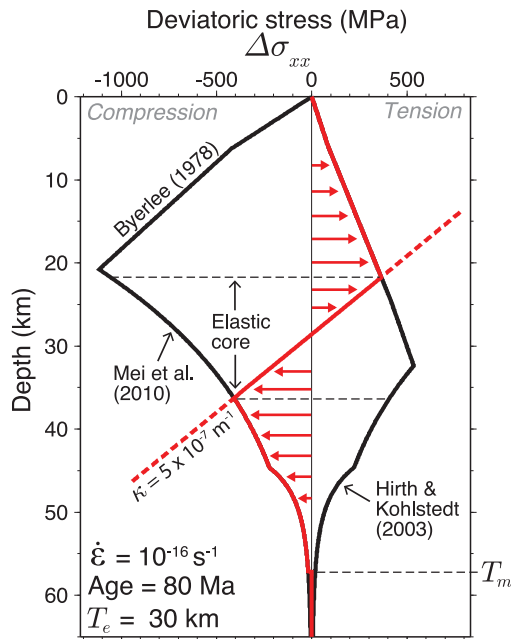
Fig. 14 shows the formulation of the YSE used in this study. The YSE at each depth increment is defined as the smallest of the three experimentally derived failure slopes (brittle, low-temperature plasticity and power-law creep), assuming a constant strain rate with depth. The LTP flow law of Katayama & Karato (2008) is for wet olivine ($810\text{--}1220 \text{ H}/10^6\text{Si}$) and therefore was used in conjunction with the wet ($1000 \text{ H}/10^6\text{Si}$) PLC law of Hirth & Kohlstedt (2003). The other LTP flow laws are for dry olivine (water content < 80

Table 2. Parameters for the low-temperature plasticity (LTP) olivine flow laws that were tested in this study. The flow laws listed as M(10⁴), M(10⁶) and M(10⁸) are weakened modifications of Mei *et al.* (2010), where A has been increased by 4, 6 and 8 orders of magnitude, respectively.

LTP flow law	A (s ⁻¹ MPa ⁻ⁿ)	n	H_0^* (kJ mol ⁻¹)	σ_P (GPa)	p	q
Goetze (1978)	5.7×10^{11}	0	536	8.5	1	2
Evans & Goetze (1979)	1.4×10^{12}	0	499	9.1	1	2
Raterron <i>et al.</i> (2004)	2.6×10^{12}	0	564	15.4	2/3	2
Katayama & Karato (2008)	$1.0 \times 10^{7.8}$	2	518	2.87	1	2
Mei <i>et al.</i> (2010)	1.4×10^{-7}	2	320	5.9	1/2	1
M(10 ⁴)	1.4×10^{-3}	2	320	5.9	1/2	1
M(10 ⁶)	1.4×10^{-1}	2	320	5.9	1/2	1
M(10 ⁸)	1.4×10^1	2	320	5.9	1/2	1

Table 3. Parameters for the power-law creep (PLC) olivine flow laws used in this study. Note that for wet olivine, B was calculated for a water concentration of 1000 H/10⁶Si.

PLC flow law	B (s ⁻¹ MPa ⁻ⁿ)	n	E^* (kJ mol ⁻¹)	V^* (10 ⁻⁶ m ³ mol ⁻¹)
Hirth & Kohlstedt (2003) - dry	1.10×10^5	3.5	530	14
Hirth & Kohlstedt (2003) - wet	3.58×10^5	3.5	480	11

**Figure 14.** Figure illustrating the YSE and the calculation of the predicted T_e . The YSE (black) is defined as the smallest of the three experimentally derived failure slopes (brittle, low-temperature plasticity and power-law creep), assuming a constant strain rate with depth. To calculate the predicted T_e , an elastic bending stress profile is calculated for a given curvature, κ (dashed red). This is then truncated by the YSE to give the bending stress under the assumption of elastic-perfectly plastic deformation (solid red). This stress distribution can then be used to calculate the bending moment and predicted T_e .

H/10⁶Si; Mei & Kohlstedt 2000), and were therefore used in conjunction with the dry PLC law of Hirth & Kohlstedt (2003). Fig. 13 shows that the LTP strength curves of Goetze (1978), Evans & Goetze (1979) and Raterron *et al.* (2004) do not intersect the dry-olivine PLC curve of Hirth & Kohlstedt (2003). Therefore, for these laws, we linearly interpolated between the points at which the LTP strength is 200 MPa and the PLC strength is 100 MPa, as this is the range over which the transition from LTP to PLC appears to occur (Goetze 1978; Evans & Goetze 1979). As the brittle yield stress is strongly pressure dependent and the ductile yield stress is strongly

temperature dependent, there is a transition from brittle to ductile deformation with increasing depth.

The YSEs for each circum-Pacific trench-outer rise profile were calculated assuming a plate-cooling geotherm for the average seafloor age 100 km from the trench axis. The bin-averaged strain rate was estimated using the rate of change of plate curvature and the subduction velocity:

$$\dot{\epsilon} = y^* \frac{d\kappa}{dt} = y^* V_s \frac{d\kappa}{dx}, \quad (13)$$

where y^* is a particular distance from the neutral surface of bending, κ is curvature, t is time, V_s is the subduction velocity and x is distance. $\frac{d\kappa}{dx}$ was calculated from the best-fitting uniform T_e elastic plate model and then averaged over the 200 km closest to the trench axis. V_s was calculated as the sum of the trench-normal plate convergence velocity (MORVEL plate motion model, DeMets *et al.* 2010) and the backarc deformation rate (Heuret & Lallemand 2005). y^* was chosen as the depth to the 200 °C plate-cooling isotherm based on the seafloor age. This depth is intermediate between the neutral surface and the plate surface and also accounts for the increase in mechanical thickness with plate age.

The YSE can be used to predict the T_e for an assumed plate curvature, under the assumption that the lithosphere behaves as an elastic-perfectly plastic material. The elastic bending stress in a plate flexed to curvature κ is (dashed red line in Fig. 14):

$$\Delta\sigma_{xx}^{\text{elast}} = \frac{E(y - y_n)\kappa}{1 - \nu^2}, \quad (14)$$

where y_n is the depth of the neutral surface. This is then truncated by the YSE (solid red line in Fig. 14) and the resultant stress distribution, $\Delta\sigma_{xx}$, is used to calculate the bending moment:

$$M = \int_0^{T_m} \Delta\sigma_{xx}(y - y_n) dy, \quad (15)$$

where T_m is the mechanical thickness, defined as the depth at which the yield strength falls below 1 per cent of the overburden pressure (Cloetingh & Burov 1996). This is then used to calculate the flexural rigidity and T_e using eqs (3) and (2), respectively.

Fig. 15 shows the predicted T_e as a function of plate curvature for each of the YSEs used in this study and for a range of plate ages. The figure shows that T_e decreases with increasing $|\kappa|$ due to brittle and ductile failure, and that the rate of decrease slows with increasing $|\kappa|$. The figure also shows that the predicted T_e is

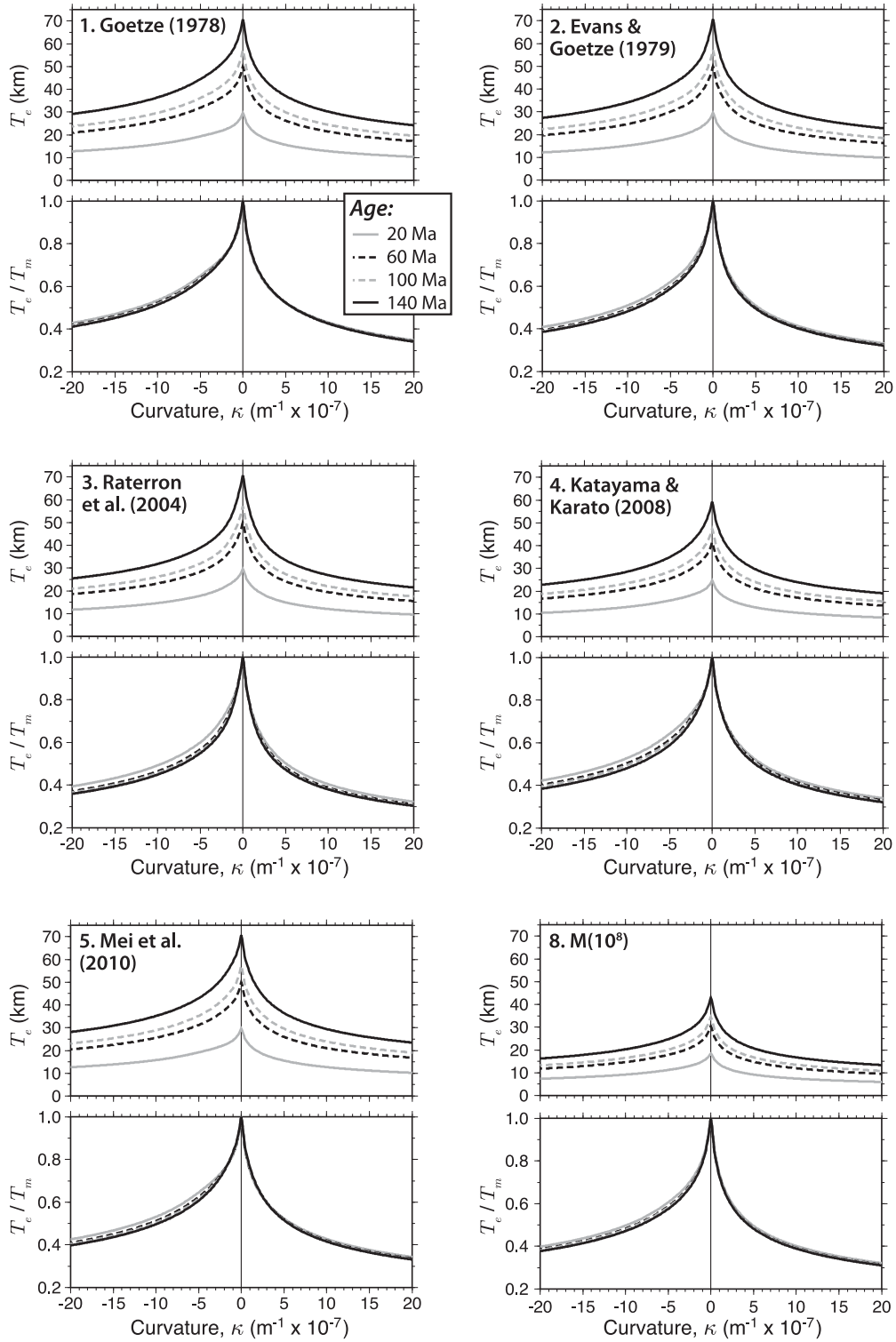


Figure 15. Predicted T_e versus plate curvature for each of the YSEs used in this study and for a range of plate ages. The LTP flow law used to construct the YSE is labelled in the top left of each pair of plots; the laws are numbered as in Fig. 13. The upper plots show predicted T_e and the lower plots show predicted T_e as a fraction of the initial mechanical thickness, T_m . All YSEs were calculated with strain rate 10^{-16} s^{-1} .

higher for negative than for positive curvatures. This is because negative curvature implies compression of the uppermost, brittle lithosphere, and the brittle yield strength is higher in compression than in tension. Fig. 15 shows that although the decrease in T_e is larger for older plates (upper plots), the reduction in T_e as a fraction of the initial mechanical thickness is nearly independent of plate age

(lower plots). This is in agreement with our finding from Inversion A2 that there is no correlation between plate weakening and plate age.

An appropriate plate curvature was required to calculate the predicted T_e for each circum-Pacific trench-outer rise profile. We chose to use the maximum curvature of the best-fitting uniform T_e elastic

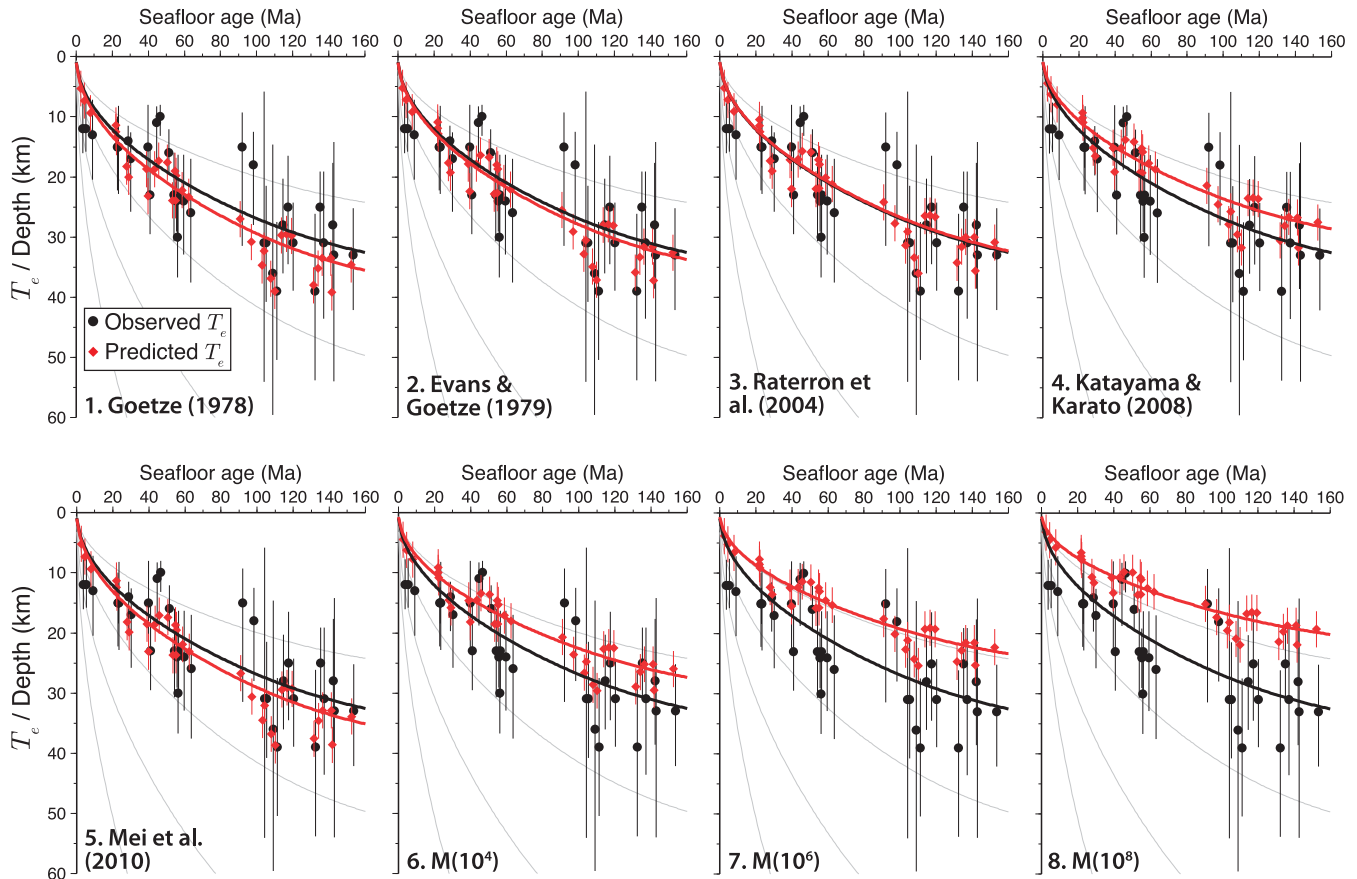


Figure 16. For the circum-Pacific segment-bins, the predicted T_e (red diamonds) and the observed T_e from Inversion A1 (black dots) plotted against seafloor age. The LTP flow law used to calculate the predicted T_e is labelled on each plot; in all cases, the brittle regime was calculated with Byerlee's (1978) friction coefficients and hydrostatic PFP. The grey curves show the depths to the 300, 600, 900 and 1200 °C cooling plate model isotherms. The isotherms that best fit the observed T_e and predicted T_e are shown in black and red, respectively. The LTP flow laws are numbered as in Fig. 13.

plate model, as Mueller & Phillips (1995) found that this best recovered the input rheology of a synthetic data set. The predicted T_e was then compared to the observed T_e , as derived from Inversion A1, in an effort to constrain mantle rheology.

In the first analysis, the brittle regime for all YSEs was calculated using Byerlee's (1978) friction coefficients (eq. 10) and a hydrostatic PFP. We assumed hydrostatic PFP because there is evidence that bend-faults on the outer trench-slope facilitate significant hydration of the crust and uppermost mantle (e.g. Yamano & Uyeda 1990; Ranero *et al.* 2003; Grevemeyer *et al.* 2007).

Fig. 16 compares the observed T_e derived from the segment-bins to the predicted T_e based on YSEs for different assumed LTP flow laws. Fig. 17(a) shows the RMSE between the observed and predicted T_e (left plot), and a comparison between the best-fitting isotherms to the observed and predicted T_e (right plot).

Figs 16 and 17(a) show that for the segment-bins, the LTP flow laws that best predict the observed T_e are Evans & Goetze (1979) and Raterron *et al.* (2004), which yield RMSE <4.6 km and a best-fitting oceanic isotherm of 414 and 398 °C, respectively. This compares well to the best-fitting isotherm to the observed T_e of 400 °C. The LTP laws of Goetze (1978) and Mei *et al.* (2010) also appear to provide a good fit to the observed segment-bin T_e , with RMSE <5.1 km and best-fitting isotherms that are within the 95 per cent confidence interval of the best-fitting isotherm to the observed T_e . The laws of Katayama & Karato (2008) and $M(10^4)$ also provide a reasonably good fit to the observed T_e , with RMSE <6 km, but

their best-fitting oceanic isotherms are just below the 95 per cent confidence interval of the observed best-fitting isotherm, suggesting that these laws are slightly too weak. Similar results were obtained for the trench bins.

Figs 16 and 17(a) show that the LTP flow laws that yield the worst fit to the observed T_e are cases $M(10^6)$ and $M(10^8)$, which are weakened modifications of Mei *et al.* (2010) where A has been increased by 6 and 8 orders of magnitude, respectively. These laws yield the highest RMSE between the predicted and observed T_e , >8.3 km and >6.5 km for the segment-bins and trench-bins, respectively, and the best-fitting isotherms are much lower (< 290 °C) than the best fit to the observed T_e . This suggests that these flow laws are much too weak to fit the observations.

Byerlee (1978) suggests that most rock types have similar friction coefficients, but several authors have suggested that faults are much weaker in natural systems than predicted by rock friction experiments. In particular, Craig *et al.* (2014) recently used earthquake focal mechanisms from the outer rise to suggest that the friction coefficient, μ_f , of newly formed trench-parallel bend faults is ≤ 0.3 . They suggest that this may be due to the formation of weak clay minerals by hydrothermal alteration when the oceanic crust was created at the MOR. Another possibility is serpentinization in the olivine-rich upper mantle by fluids which penetrate outer rise bend faults. Other authors have shown some continental fault zones to be similarly weak (e.g. Zoback *et al.* 1987; Middleton & Copley 2014).

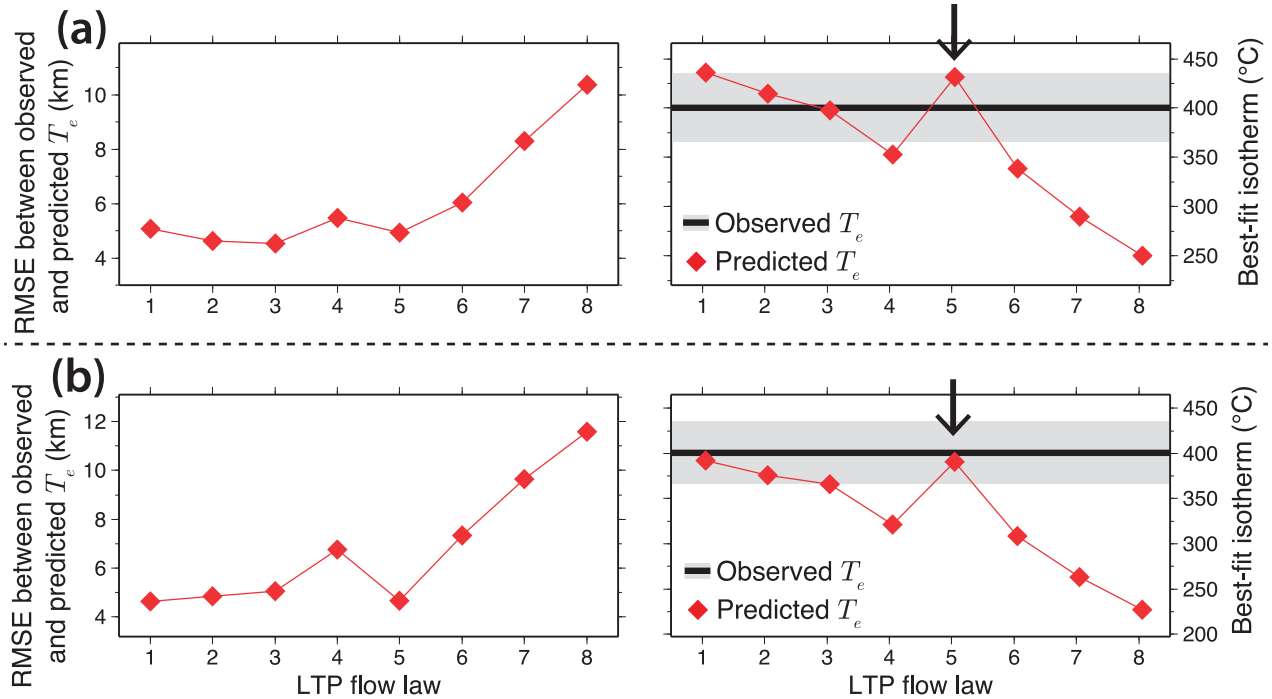


Figure 17. Statistics comparing the observed T_e from Inversion A1 in segment-bins to the calculated T_e assuming (a) Byerlee's (1978) friction coefficients and hydrostatic PFP and (b) $\mu_f = 0.3$ and hydrostatic PFP. The left plots show the RMSE between the observed T_e and the predicted T_e for each LTP flow law. The right plots show the best-fitting isotherm to the observed T_e (black line, where the grey shade is the 95 per cent confidence interval), and the best-fitting isotherm to the predicted T_e for each LTP flow law (red diamonds). The LTP flow laws are numbered as in Fig. 13.

As a result of these findings, we repeated the YSE analysis using $\mu_f = 0.3$ instead of Byerlee's coefficients, where PFP is once again hydrostatic (Fig. 17b). This causes the predicted T_e to be systematically lower, but only by a mean of 1.7 ± 0.5 km for young lithosphere (<80 Ma) and 2.9 ± 0.3 km for old lithosphere (>80 Ma). As a result, whilst there is some trade-off between friction coefficient and the best-fitting LTP flow law, it is not a major factor.

Fig. 17(b) shows that the flow laws that best predict the observed T_e are the dry olivine LTP flow laws of Goetze (1978), Evans & Goetze (1979), Raterron *et al.* (2004) and Mei *et al.* (2010). These laws yield RMSE <5.1 and <3.8 km for the segment-bins and trench-bins, respectively, and best-fitting oceanic isotherms that are within the 95 per cent confidence interval of the best-fit to the observed T_e . The weakened Mei *et al.* (2010) cases of $M(10^4)$, $M(10^6)$ and $M(10^8)$ yield the worst fit to the observed T_e , with RMSE >7.4 km for the segment-bins and >5.5 km for the trench-bins. The best-fitting oceanic isotherms to the predicted T_e for these laws, that range from 230 to 310 °C, are much too low to fit the best fit to the observed T_e of 400 and 380 °C for the segment-bins and trench-bins, respectively. This suggests that these flow laws are too weak to fit the observations. Since $\mu_f = 0.3$ has been constrained by observations from oceanic outer rises, we consider this to be more reliable than Byerlee's coefficients and therefore these are our preferred values.

8.4 Comparison of the mantle rheology at circum-Pacific subduction zones and the Hawaiian Islands

We have used laboratory-derived YSEs and modelled plate curvatures to constrain mantle rheology at the trench-outer rise system of circum-Pacific subduction zones, and in particular the rheology in the LTP regime. Regardless of the assumed friction coefficient,

the dry-olivine LTP flow laws of Goetze (1978), Evans & Goetze (1979), Raterron *et al.* (2004) and Mei *et al.* (2010) all provide a satisfactory fit to the observed T_e . This might appear surprising given that Zhong & Watts (2013) found that these laws are much too strong to fit observations of flexure at the Hawaiian Islands in the interior of the Pacific oceanic plate.

Zhong & Watts (2013) calculated the deformation due to volcano loading using a 3-D finite-element viscoelastic model, where the effective viscosity was prescribed by failure laws for frictional sliding, LTP and PLC. By isolating the time-dependent load of the Hawaiian Islands and comparing calculations to observations of seismically constrained crustal flexure and the depth-dependence of seismicity, they were able to constrain upper mantle rheology. They found that while their results are insensitive to the PLC regime and, like us, fairly insensitive to the friction coefficient, the published LTP flow laws, including that of Mei *et al.* (2010), are much too strong to fit the observed crustal flexure. Zhong & Watts (2013) therefore weakened Mei *et al.* (2010) by increasing A , finding that in order to fit the observations, it must be increased by 6–8 orders of magnitude depending on the assumed friction coefficient. This contrasts with our results from the circum-Pacific subduction zones, which suggest that $M(10^6)$ and $M(10^8)$ are much too weak to fit the observed T_e . This discrepancy can be expressed in another way by stating that Pacific oceanic mantle lithosphere appears weaker for its age at the Hawaiian Islands than at subduction zones.

We are not certain of the origin of such a difference in rheological properties between the Pacific plate boundary and its interior. One possibility is a difference in modelling approach. However, we have applied our YSE-based approach to Hawaii and obtained similar results regarding the best fit flow law as did Zhong & Watts (2013). In particular, we derived the observed T_e (26 km) by modelling seismically constrained crustal deflections using a 3-D elastic plate,

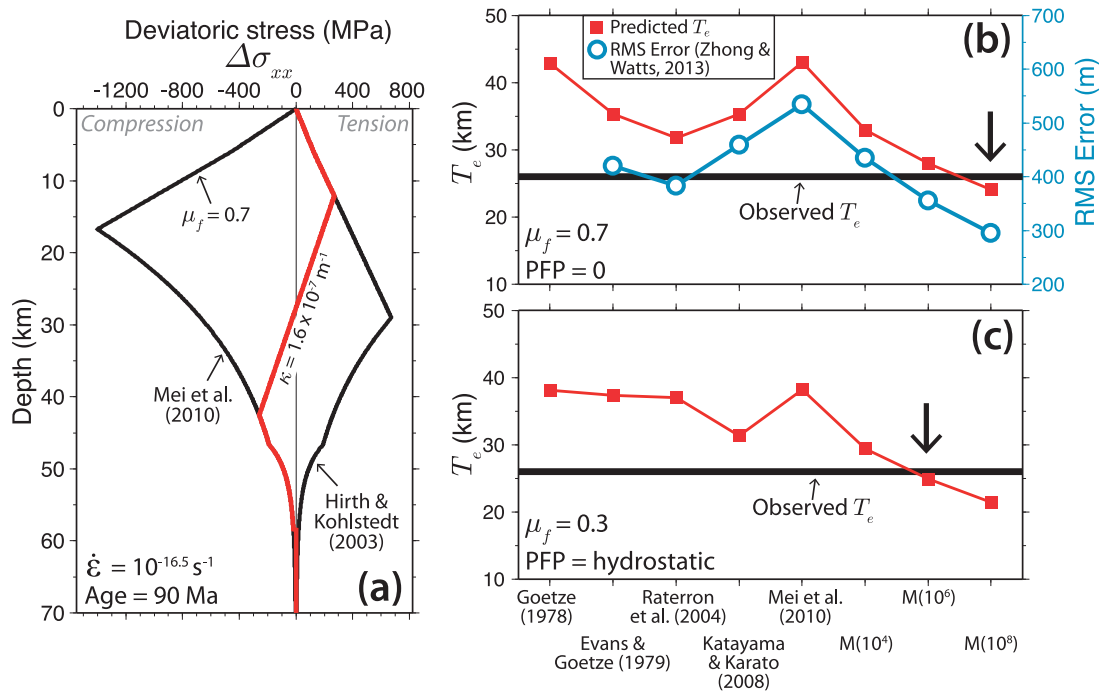


Figure 18. Comparison between the results of the YSE-based method used in this study and those of Zhong & Watts (2013) at the Hawaiian Islands. (a) The YSE (black) and stress distribution (red) that were used to calculate the predicted T_e for the LTP law of Mei *et al.* (2010) assuming $\mu_f = 0.7$ and zero PFP. (b) The observed T_e (black line) compared to the predicted T_e for each LTP flow assuming $\mu_f = 0.7$ and zero PFP. Also shown for comparison is the RMSE between the observed and calculated crustal deflections from the study of Zhong & Watts (2013) (blue circles). (c) The observed T_e compared to the predicted T_e assuming $\mu_f = 0.3$ and hydrostatic PFP. Note that in Fig. 18(b), in keeping with the study of Zhong & Watts (2013), we have not interpolated between the LTP and PLC regimes for the laws of Evans & Goetze (1979) and Raterron *et al.* (2004). The LTP flow laws are numbered as in Fig. 13.

and used the maximum ridge-normal plate curvature to calculate the predicted T_e (Appendix C). To calculate the YSEs (e.g. Fig. 18a), we assumed a plate cooling geotherm for 90 Ma lithosphere and estimated the strain rate by assuming that the plate curvature accrued linearly over the shield to post-shield volcano building phase on Oahu (4–2 Ma).

Fig. 18(b) shows that if we assume $\mu_f = 0.7$ and zero PFP, the results of the YSE-based method and those of Zhong & Watts (2013) are very similar. The LTP law of Mei *et al.* (2010) is much too strong in both cases, such that A must be increased by 6–8 orders of magnitude. This gives us confidence then that the discrepancy is not due to differences in modelling approach. Note that in Fig. 18(b), in keeping with the study of Zhong & Watts (2013), we have not interpolated between the LTP and PLC regimes for the laws of Evans & Goetze (1979) and Raterron *et al.* (2004). Fig. 18(c) shows that if we assume $\mu_f = 0.3$ and hydrostatic PFP, our YSE-based method suggests that Mei *et al.* (2010) is still too strong and A must be increased by ~ 6 orders of magnitude. This result contrasts strongly with our results from circum-Pacific subduction zones (Fig. 17).

One possible cause of the discrepancy in rheology is differences in the timescales of loading. There is evidence that oceanic lithosphere responds as a viscoelastic plate to loading, and Watts & Zhong (2000) used observations of ocean island and seamount volcanism to show that following loading, it takes approximately 1–2 Myr for oceanic lithosphere to relax to its long-term elastic thickness. At the trench-outer rise of subduction zones, the subducting plate is continuously bending such that much of the strain has accumulated within the past 100 kyr or so, and thus there may be significant unrelaxed viscoelastic stresses (Farrington *et al.* 2014) that remain in the plate. In contrast, the Hawaiian island of Oahu was emplaced in

a discrete burst of volcanism 4–2 Ma, allowing enough time for most of the viscoelastic stresses to have relaxed. This might explain why the lithosphere appears rheologically stronger at subduction zones than at Hawaii, as the YSE-based method used in this study assumes elastic-plastic behavior and thus does not specifically account for the effects of viscoelasticity at the trench-outer rise.

Another possibility is that Pacific oceanic lithosphere has been thermally rejuvenated and therefore weakened by the impinging Hawaiian plume. However, Von Herzen *et al.* (1989) showed that there is no systematic increase in heat flow along or across the Hawaiian swell, suggesting predominantly dynamic support and only small temperature anomalies (< 100 – 200 °C) in the lower lithosphere. Alternatively, Wessel (1992) suggested that interference between flexural stresses and thermal bending stresses, which accrue as the lithosphere cools away from the MOR, might cause the lithosphere beneath seamounts and ocean islands to appear weaker than at the trench-outer rise. Finally, ‘magma-assisted flexure’ might also explain the relative weakness of the oceanic lithosphere, as magmatic dikes beneath the Hawaiian islands may accommodate flexure at smaller differential stresses than ductile rock yielding (Buck *et al.* 2015).

9 CONCLUSIONS

(1) We have used ensemble averages of a high-resolution grid of free-air gravity anomaly, together with an inverse modelling technique, to determine the effective elastic thickness, T_e , of circum-Pacific subducting oceanic lithosphere and its relationship to plate age.

(2) Synthetic modelling tests that take into account noise in the free-air gravity and bathymetry data show that T_e can be recovered

best if we use free-air gravity anomaly, rather than bathymetry, data and ensemble-averaged profiles that are at least 750 km long.

(3) Inverse modelling using a uniform T_e elastic plate suggests that T_e increases with age of the subducting oceanic lithosphere. T_e is given approximately by the depth to the 400 °C (segment-bin) and 380 °C (trench-bin) oceanic isotherm, based on a plate cooling model.

(4) The fits between observed and calculated free-air gravity anomalies are significantly improved if a mechanically weak zone is included between the trench axis and the outer rise. This weak zone is coincident with observations of bend-faulting, seismicity and hydration of the uppermost mantle.

(5) Inverse modelling shows that T_e landward of the outer rise (landward T_e) is generally 40–65 per cent less than the T_e seaward of the outer rise (seaward T_e). Both landward and seaward T_e increases with age of the subducting oceanic lithosphere and are given by the depth to the 342–349 and 671–714 °C oceanic isotherm, respectively, based on a cooling plate model.

(6) A dependence of T_e on age is consistent with models for the cooling of oceanic lithosphere as it moves away from a mid-ocean ridge and the temperature-dependent ductile creep of lithospheric minerals such as olivine.

(7) The discrepancy between this study and that of Bry & White (2007) can be explained by a combination of factors which include: the manner of long wavelength gravity field removal; the method used to calculate the modelled gravity anomalies; the constraint placed on M_0 ; and the location assumed for the trench axis.

(8) By comparing the observed T_e to the predicted T_e based on laboratory-derived YSEs and an assumption of elastic-perfectly plastic deformation, we have attempted to constrain the rheology of oceanic lithosphere.

(9) Regardless of the assumed friction coefficient, the dry-olivine LTP flow laws of Goetze (1978), Evans & Goetze (1979), Raterron *et al.* (2004) and Mei *et al.* (2010) all provide quite a good fit to the observed T_e at circum-Pacific subduction zones. This contrasts with the Hawaiian Islands, where these flow laws are much too strong to fit the observations.

(10) This discrepancy in rheology may be caused by differences in the timescale of loading and therefore the amount of viscoelastic stress relaxation that has occurred. Other possibilities include thermal rejuvenation and magma-assisted flexure at the Hawaiian Islands.

ACKNOWLEDGEMENTS

We thank Dan Bassett (Scripps Institution of Oceanography) for his help in the preparation of the ensemble profiles, Pål Wessel and anonymous reviewer for their helpful comments on an early version of the paper and NERC grants NE/F005318/1 and NE/I026839/1 for support. JH was funded by a NERC tied studentship. All figures were constructed using GMT (Wessel & Smith 1998).

REFERENCES

- Barrell, J., 1914. The strength of the Earth's crust, *J. Geol.*, **22**, 655–683.
- Bassett, D. & Watts, A.B., 2015. Gravity anomalies, crustal structure, and seismicity at subduction zones: 1. Seafloor roughness and subducting relief, *Geochem. Geophys. Geosyst.*, **16**(5), 1508–1540.
- Bell, T.H., 1975. Statistical features of sea-floor topography, *Deep Sea Res.*, **22**, 883–892.
- Billen, M., Cowgill, E. & Buer, E., 2007. Determination of fault friction from reactivation of abyssal-hill faults in subduction zones, *Geology*, **35**(9), 819–822.
- Billen, M.I. & Gurnis, M., 2005. Constraints on subducting plate strength within the Kermadec trench, *J. geophys. Res.*, **110**(B5), doi:10.1029/2004JB003308.
- Bodine, J.H. & Watts, A.B., 1979. On lithospheric flexure seaward of the Bonin and Mariana trenches, *Earth planet. Sci. Lett.*, **43**(1), 132–148.
- Bodine, J.H., Steckler, M.S. & Watts, A.B., 1981. Observations of flexure and the rheology of the oceanic lithosphere, *J. geophys. Res.*, **86**(B5), 3695–3707.
- Bott, M.H.P., 1960. The use of rapid digital computing methods for direct gravity interpretation of sedimentary basins, *Geophys. J. R. Astr. Soc.*, **3**, 63–67.
- Bry, M. & White, N., 2007. Reappraising elastic thickness variation at oceanic trenches, *J. geophys. Res.*, **112**(8), doi:10.1029/2005JB004190.
- Buck, W.R., Lavie, L.L. & Choi, E., 2015. Magma explains low estimates of lithospheric strength based on flexure of ocean island loads, in *EGU General Assembly Conference Abstracts*, 2015 April 12–17, Vienna, Austria.
- Bürgmann, R., Kogan, M.G., Steblov, G.M., Hilley, G., Levin, V.E. & Apel, E., 2005. Interseismic coupling and asperity distribution along the Kamchatka subduction zone, *J. geophys. Res.*, **110**(B7), doi:10.1029/2005JB003648.
- Burov, E.B. & Diament, M., 1995. The effective elastic thickness (T_e) of continental lithosphere: what does it really mean?, *J. geophys. Res.*, **100**(B3), 3905–3927.
- Byerlee, J., 1978. Friction of rocks, *Pure appl. Geophys.*, **116**(4–5), 615–626.
- Caldwell, J.G. & Turcotte, D.L., 1979. Dependence of the thickness of the elastic oceanic lithosphere on age, *J. geophys. Res.*, **84**(B13), 7572–7576.
- Caldwell, J.G., Haxby, W.F., Karig, D.E. & Turcotte, D.L., 1976. On the applicability of a universal elastic trench profile, *Earth planet. Sci. Lett.*, **31**(2), 239–246.
- Capitanio, F.A., Morra, G. & Goes, S., 2009. Dynamics of plate bending at the trench and slab-plate coupling, *Geochem. Geophys. Geosyst.*, **10**, 4, doi:10.1029/2008GC002348.
- Cardozo, N., 2009. 3D flexural modeling code, Available at: <http://www.ux-uis.no/~nestor/work/matlabScripts.html>
- Chapman, M.E., 1979. Techniques for interpretation of geoid anomalies, *J. geophys. Res.*, **84**(B8), 3793–3801.
- Chapple, W.M. & Forsyth, D.W., 1979. Earthquakes and bending of plates at trenches, *J. geophys. Res.*, **84**(B12), 6729–6749.
- Chopra, P.N. & Paterson, M.S., 1984. The role of water in the deformation of dunite, *J. geophys. Res.*, **89**(B9), 7861–7876.
- Christensen, D.H. & Ruff, L.J., 1988. Seismic coupling and outer rise earthquakes, *J. geophys. Res.*, **93**(B11), 13 421–13 444.
- Cloetingh, S. & Burov, E.B., 1996. Thermomechanical structure of European continental lithosphere: constraints from rheological profiles and EET estimates, *Geophys. J. Int.*, **124**(3), 695–723.
- Cochran, J.R., 1979. An analysis of isostasy in the world's oceans: 2. Mid-ocean ridge crests, *J. geophys. Res.*, **84**(B9), 4713–4729.
- Contreras-Reyes, E. & Osses, A., 2010. Lithospheric flexure modelling seaward of the Chile trench: implications for oceanic plate weakening in the Trench Outer Rise region, *Geophys. J. Int.*, **182**(1), 97–112.
- Contreras-Reyes, E., Grevemeyer, I., Flueh, E.R. & Reichert, C., 2008a. Upper lithospheric structure of the subduction zone offshore of southern Arauco peninsula, Chile, at ~38 S, *J. geophys. Res.*, **113**(B7), doi:10.1029/2007JB005569.
- Contreras-Reyes, E., Grevemeyer, I., Flueh, E.R., Scherwath, M. & Bialas, J., 2008b. Effect of trench-outer rise bending-related faulting on seismic Poisson's ratio and mantle anisotropy: a case study offshore of Southern Central Chile, *Geophys. J. Int.*, **173**(1), 142–156.
- Contreras-Reyes, E., Grevemeyer, I., Watts, A.B., Flueh, E.R., Peirce, C., Moeller, S. & Papenberg, C., 2011. Deep structure of the Tonga subduction zone: Implications for mantle hydration, tectonic erosion and arc magmatism, *J. geophys. Res.*, **116**, doi:10.1029/2011JB008434.

- Craig, T.J., Copley, A. & Jackson, J., 2014. A reassessment of outer-rise seismicity and its implications for the mechanics of oceanic lithosphere, *Geophys. J. Int.*, **197**(1), 63–89.
- Davies, G.F., 1981. Regional compensation of subducted lithosphere: effects on geoid, gravity and topography from a preliminary model, *Earth planet. Sci. Lett.*, **54**(3), 431–441.
- De Bremaecker, J.-C., 1977. Is the oceanic lithosphere elastic or viscous?, *J. geophys. Res.*, **82**(14), 2001–2004.
- DeMets, C., Gordon, R.G. & Argus, D.F., 2010. Geologically current plate motions, *Geophys. J. Int.*, **181**(1), 1–80.
- Dengo, C.A. & Logan, J.M., 1981. Implications of the mechanical and frictional behavior of serpentinite to seismogenic faulting, *J. geophys. Res.*, **86**(B11), 10 771–10 782.
- Divins, D.L., 2003. *Total Sediment Thickness of the World's Oceans & Marginal Seas*, NOAA National Geophysical Data Center, Boulder, CO.
- Edmond, J.M. & Paterson, M.S., 1972. Volume changes during the deformation of rocks at high pressures, *Int. J. Rock Mech. Min. Sci. Geomech. Abstracts*, **9**(2), 161–182.
- Escartin, J., Hirth, G. & Evans, B., 1997. Nondilatant brittle deformation of serpentinites: implications for Mohr-Coulomb theory and the strength of faults, *J. geophys. Res.*, **102**(B2), 2897–2913.
- Escartin, J., Hirth, G. & Evans, B., 2001. Strength of slightly serpentinized peridotites: implications for the tectonics of oceanic lithosphere, *Geology*, **29**(11), 1023–1026.
- Evans, B. & Goetze, C., 1979. The temperature variation of hardness of olivine and its implication for polycrystalline yield stress, *J. geophys. Res.*, **84**(B10), 5505–5524.
- Farrington, R.J., Moresi, L.-N. & Capitanio, F.A., 2014. The role of viscoelasticity in subducting plates, *Geochem. Geophys. Geosyst.*, **15**(11), 4291–4304.
- Forsyth, D. & Uyeda, S., 1975. On the relative importance of the driving forces of plate motion, *Geophys. J. Int.*, **43**(1), 163–200.
- Froehlich, C., Billington, S., Engdahl, E.R. & Malahoff, A., 1982. Detection and location of earthquakes in the central Aleutian subduction zone using island and ocean bottom seismograph stations, *J. geophys. Res.*, **87**(B8), 6853–6864.
- García, E.S., Sandwell, D.T. & Luttrell, K.M., 2015. An iterative spectral solution method for thin elastic plate flexure with variable rigidity, *Geophys. J. Int.*, **200**(2), 1010–1026.
- García-Castellanos, D., Torne, M. & Fernandez, M., 2000. Slab pull effects from a flexural analysis of the Tonga and Kermadec trenches (Pacific Plate), *Geophys. J. Int.*, **141**(2), 479–484.
- Gilbert, G.K., 1890. *Lake Bonneville*, US Government Printing Office.
- Goetze, C., 1978. The mechanisms of creep in olivine [and discussion], *Phil. Trans. R. Soc. Lond. A, Math. Phys. Sci.*, **288**(1350), 99–119.
- Goetze, C. & Evans, B., 1979. Stress and temperature in the bending lithosphere as constrained by experimental rock mechanics, *Geophys. J. Int.*, **59**(3), 463–478.
- Grevemeyer, I., Kaul, N., Diaz-Naveas, J.L., Villinger, H.W., Ranero, C.R. & Reichert, C., 2005. Heat flow and bending-related faulting at subduction trenches: case studies offshore of Nicaragua and Central Chile, *Earth planet. Sci. Lett.*, **236**(1), 238–248.
- Grevemeyer, I., Ranero, C.R., Flueh, E.R., Kläschen, D. & Bialas, J., 2007. Passive and active seismological study of bending-related faulting and mantle serpentinization at the Middle America trench, *Earth planet. Sci. Lett.*, **258**(3), 528–542.
- Griggs, D.T., 1972. The sinking lithosphere and the focal mechanism of deep earthquakes, in *The Nature of the Solid Earth*, pp. 361–384, McGraw-Hill.
- Gunn, R., 1943. A quantitative evaluation of the influence of the lithosphere on the anomalies of gravity, *J. Franklin Inst.*, **236**(1), 47–66.
- Hanks, T.C., 1971. The Kuril Trench-Hokkaido Rise system: large shallow earthquakes and simple models of deformation, *Geophys. J. Int.*, **23**(2), 173–189.
- Hayes, D.E. & Ewing, M., 1970. Pacific boundary structure, in *The Sea*, pp. 29–72, ed. Maxwell, A.E., John Wiley & Sons.
- Hayes, G.P., Wald, D.J. & Johnson, R.L., 2012. Slab1.0: a three-dimensional model of global subduction zone geometries, *J. geophys. Res.*, **117**(B1), doi:10.1029/2011JB008524.
- Heuret, A. & Lallemand, S., 2005. Plate motions, slab dynamics and back-arc deformation, *Phys. Earth planet. Inter.*, **149**(1), 31–51.
- Hirth, G. & Kohlstedt, D.L., 1996. Water in the oceanic upper mantle: implications for rheology, melt extraction and the evolution of the lithosphere, *Earth planet. Sci. Lett.*, **144**(1), 93–108.
- Hirth, G. & Kohlstedt, D., 2003. Rheology of the upper mantle and the mantle wedge: a view from the experimentalists, in *Inside the Subduction Factory*, ed. Eiler, J. pp. 83–105, American Geophysical Union.
- IOC, IHO & BODC, 2003. *Centenary Edition of the GEBCO Digital Atlas*, published on CD-ROM on behalf of the Intergovernmental Oceanographic Commission and the International Hydrographic Organization as part of the General Bathymetric Chart of the Oceans, British Oceanographic Data Centre.
- Isacks, B.L. & Barazangi, M., 1977. Geometry of Benioff zones, in *Island Arcs, Deep Sea Trenches and Back-Arc Basins*, eds Talwani, M. & Pitman, W.C., pp. 99–114, American Geophysical Union.
- Ivandić, M., Grevemeyer, I., Berhorst, A., Flueh, E.R. & McIntosh, K., 2008. Impact of bending related faulting on the seismic properties of the incoming oceanic plate offshore of Nicaragua, *J. geophys. Res.*, **113**(B5), doi:10.1029/2007JB005291.
- Jeffreys, H., 1926. On the nature of isostasy, *Gerl. Beitr. Geophys.*, **15**(2), 167–186.
- Jones, G.M., Hilde, T.W.C., Sharman, G.F. & Agnew, D.C., 1978. Fault patterns in outer trench walls and their tectonic significance, *J. Phys. Earth*, **26**(Suppl.), S85–S101.
- Judge, A.V. & McNutt, M.K., 1991. The relationship between plate curvature and elastic plate thickness: a study of the Peru-Chile Trench, *J. geophys. Res.*, **96**(B10), 16 625–16 639.
- Karato, S. & Wu, P., 1993. Rheology of the upper mantle: a synthesis, *Science*, **260**(5109), 771–778.
- Katayama, I. & Karato, S., 2008. Low-temperature, high-stress deformation of olivine under water-saturated conditions, *Phys. Earth planet. Inter.*, **168**(3), 125–133.
- Kobayashi, K., Nakanishi, M., Tamaki, K. & Ogawa, Y., 1998. Outer slope faulting associated with the western Kuril and Japan trenches, *Geophys. J. Int.*, **134**(2), 356–372.
- Kocks, W.F., 1975. *Thermodynamics and Kinetics of Slip*, Vol. 19: *Progress in Materials Science Thermodynamics and Kinetics of Slip*, pp. 291, Pergamon Press.
- Kohlstedt, D.L., Evans, B. & Mackwell, S.J., 1995. Strength of the lithosphere: constraints imposed by laboratory experiments, *J. geophys. Res.*, **100**(B9), 17 587–17 602.
- Levitt, D.A. & Sandwell, D.T., 1995. Lithospheric bending at subduction zones based on depth soundings and satellite gravity, *J. geophys. Res.*, **100**(B1), 379–400.
- Manriquez, P., Contreras-Reyes, E. & Osses, A., 2014. Lithospheric 3-D flexure modelling of the oceanic plate seaward of the trench using variable elastic thickness, *Geophys. J. Int.*, **196**(2), 681–693.
- Mareschal, J.-C., 1989. Fractal reconstruction of sea-floor topography, *Pure appl. Geophys.*, **131**(1–2), 197–210.
- Markwardt, C.B., 2009. Non-linear least squares fitting in IDL with MPFIT, in *Proceedings of the ADASS XVIII, ASP Conference Ser.*, Vol. 411, eds Bohlender, D., Dowler, P. & Durand, D., p. 251, arXiv preprint arXiv:0902.2850.
- Massell, C.G., 2002. *Large-Scale Structural Variation of Trench Outer Slopes and Rises*, University of California.
- Masson, D.G., 1991. Fault patterns at outer trench walls, *Mar. Geophys. Res.*, **13**(3), 209–225.
- McAdoo, D.C., Caldwell, J.G. & Turcotte, D.L., 1978. On the elastic-perfectly plastic bending of the lithosphere under generalized loading with application to the Kuril Trench, *Geophys. J. Int.*, **54**(1), 11–26.
- McAdoo, D.C., Martin, C.F. & Poulouse, S., 1985. Seasat observations of flexure: evidence for a strong lithosphere, *Tectonophysics*, **116**(3), 209–222.
- McNutt, M.K., 1984. Lithospheric flexure and thermal anomalies, *J. geophys. Res.*, **89**(B13), 11 180–11 194.

- McNutt, M.K. & Menard, H.W., 1982. Constraints on yield strength in the oceanic lithosphere derived from observations of flexure, *Geophys. J. Int.*, **71**(2), 363–394.
- Mei, S. & Kohlstedt, D.L., 2000. Influence of water on plastic deformation of olivine aggregates: 2. Dislocation creep regime, *J. geophys. Res.*, **105**(B9), 21 471–21 481.
- Mei, S., Suzuki, A.M., Kohlstedt, D.L., Dixon, N.A. & Durham, W.B., 2010. Experimental constraints on the strength of the lithospheric mantle, *J. geophys. Res.*, **115**(B8), doi:10.1029/2009JB006873.
- Meinesz, F.A.V., 1941. Gravity over the Hawaiian Archipelago and over the Madeira area, conclusions about the Earth's crust, *Proc. Kon. Ned. Akad. Wetensch.*, **44**, 2–12.
- Middleton, T.A. & Copley, A., 2014. Constraining fault friction by re-examining earthquake nodal plane dips, *Geophys. J. Int.*, **196**(2), 671–680.
- Moore, D.E., Lockner, D.A., Ma, S., Summers, R. & Byerlee, J.D., 1997. Strengths of serpentinite gouges at elevated temperatures, *J. geophys. Res.*, **102**(B7), 14 787–14 801.
- Moore, J.G., 2001. Density of basalt core from Hilo drill hole, Hawaii, *J. Volcanol. Geotherm. Res.*, **112**(1), 221–230.
- Moré, J.J., 1978. The Levenberg-Marquardt algorithm: implementation and theory, *Numer. Anal.*, **630**, 105–116.
- Müller, R.D., Sdrolias, M., Gaina, C. & Roest, W.R., 2008. Age, spreading rates, and spreading asymmetry of the world's ocean crust, *Geochem. Geophys. Geosyst.*, **9**(4), 1–19.
- Mueller, S. & Phillips, R.J., 1995. On the reliability of lithospheric constraints derived from models of outer-rise flexure, *Geophys. J. Int.*, **123**(3), 887–902.
- Mueller, S., Choy, G.L. & Spence, W., 1996. Inelastic models of lithospheric stress – I. Theory and application to outer-rise plate deformation, *Geophys. J. Int.*, **125**(1), 39–53.
- Parsons, B. & Molnar, P., 1978. The origin of outer topographic rises associated with trenches, *Geophys. J. Int.*, **1**(4), 707–712.
- Parsons, B. & Sclater, J.G., 1977. An analysis of the variation of ocean floor bathymetry and heat flow with age, *J. geophys. Res.*, **82**(5), 803–827.
- Pavlis, N.K., Holmes, S.A., Kenyon, S.C. & Factor, J.K., 2012. The development and evaluation of the Earth Gravitational Model 2008 (EGM2008), *J. geophys. Res.*, **117**(B4), doi:10.1029/2011JB008916.
- Peitgen, H.-O., Saupe, D., Barnsley, M.F., Fisher, Y. & McGuire, M., 1988. *The Science of Fractal Images*, Springer.
- Raleigh, C.B. & Paterson, M.S., 1965. Experimental deformation of serpentinite and its tectonic implications, *J. geophys. Res.*, **70**(16), 3965–3985.
- Ranero, C.R. & Sallares, V., 2004. Geophysical evidence for hydration of the crust and mantle of the Nazca plate during bending at the north Chile trench, *Geology*, **32**(7), 549–552.
- Ranero, C.R., Morgan, J.P., McIntosh, K. & Reichert, C., 2003. Bending-related faulting and mantle serpentinization at the Middle America trench, *Nature*, **425**(6956), 367–373.
- Ranero, C.R., Villaseñor, A., Phipps Morgan, J. & Weinrebe, W., 2005. Relationship between bend-faulting at trenches and intermediate-depth seismicity, *Geochem. Geophys. Geosyst.*, **6**(12), doi:10.1029/2005GC000997.
- Raterron, P., Wu, Y., Weidner, D.J. & Chen, J., 2004. Low-temperature olivine rheology at high pressure, *Phys. Earth planet. Inter.*, **145**(1), 149–159.
- Richardson, R.M., 1992. Ridge forces, absolute plate motions, and the intraplate stress field, *J. geophys. Res.*, **97**(B8), 11 739–11 748.
- Sandwell, D. & Schubert, G., 1980. Geoid height versus age for symmetric spreading ridges, *J. geophys. Res.*, **85**(B12), 7235–7241.
- Sandwell, D.T., Müller, R.D., Smith, W.H.F., Garcia, E. & Francis, R., 2014. New global marine gravity model from CryoSat-2 and Jason-1 reveals buried tectonic structure, *Science*, **346**(6205), 65–67.
- Schellart, W.P., 2004. Quantifying the net slab pull force as a driving mechanism for plate tectonics, *Geophys. Res. Lett.*, **31**(7), doi:10.1029/2004GL019528.
- Seno, T. & Yamanaka, Y., 1996. Double seismic zones, compressional deep trench-outer rise events, and superplumes, in *Subduction Top to Bottom*, pp. 347–355, eds Bebout, G.E., Scholl, D.W., Kirby, S.H. & Platt, J.P., American Geophysical Union.
- Shimamoto, T., 1986. Transition between frictional slip and ductile flow for halite shear zones at room temperature, *Science*, **231**(4739), 711–714.
- Smith, W.H.F., Staudigel, H., Watts, A.B. & Pringle, M.S., 1989. The Magellan Seamounts: Early Cretaceous record of the South Pacific isotopic and thermal anomaly, *J. geophys. Res.*, **94**(B8), 10 501–10 523.
- Stesky, R.M., 1978. Mechanisms of high temperature frictional sliding in Westerly granite, *Can. J. Earth Sci.*, **15**(3), 361–375.
- Stratford, W., Peirce, C., Funnell, M., Paulatto, M., Watts, A.B., Grevemeyer, I. & Bassett, D., 2015. Effect of Seamount subduction on forearc morphology and seismic structure of the Tonga-Kermadec subduction zone, *Geophys. J. Int.*, **200**, 1503–1522.
- Talwani, M., 1971. Gravity, in *The Sea*, Vol. 4, pp. 251–297, ed. Maxwell, A.E., John Wiley & Sons.
- Tilmann, F.J., Grevemeyer, I., Flueh, E.R., Dahm, T. & Göbner, J., 2008. Seismicity in the outer rise offshore southern Chile: indication of fluid effects in crust and mantle, *Earth planet. Sci. Lett.*, **269**(1), 41–55.
- Turcotte, D.L. & Schubert, G., 1982. *Geodynamics: Applications of Continuum Physics to Geological Problems*, John Wiley & Sons, 450 pp.
- Turcotte, D.L., McAdoo, D.C. & Caldwell, J.G., 1978. An elastic-perfectly plastic analysis of the bending of the lithosphere at a trench, *Tectonophysics*, **47**(3), 193–205.
- Von Herzen, R.P., Cordery, M.J., Detrick, R.S. & Fang, C., 1989. Heat flow and the thermal origin of hot spot swells: the Hawaiian swell revisited, *J. geophys. Res.*, **94**(B10), 13 783–13 799.
- Walcott, R.I., 1970. Flexural rigidity, thickness, and viscosity of the lithosphere, *J. geophys. Res.*, **75**(20), 3941–3954.
- Watts, A.B., 1978. An analysis of isostasy in the world's oceans – 1. Hawaiian-Emperor Seamount Chain, *J. geophys. Res.*, **83**(B12), 5989–6004.
- Watts, A.B., 2001. *Isostasy and Flexure of the Lithosphere*, Cambridge Univ. Press.
- Watts, A.B. & Ribe, N.M., 1984. On geoid heights and flexure of the lithosphere at seamounts, *J. geophys. Res.: Solid Earth*, **89**(B13), 11 152–11 170.
- Watts, A.B. & Talwani, M., 1974. Gravity anomalies seaward of deep-sea trenches and their tectonic implications, *Geophys. J. Int.*, **36**(1), 57–90.
- Watts, A.B. & Talwani, M., 1975. Gravity effect of downgoing lithospheric slabs beneath island arcs, *Bull. geol. Soc. Am.*, **86**(1), 1–4.
- Watts, A.B. & ten Brink, U.S., 1989. Crustal structure, flexure, and subsidence history of the Hawaiian Islands, *J. geophys. Res.*, **94**(B8), 10 473–10 500.
- Watts, A.B. & Zhong, S., 2000. Observations of flexure and the rheology of oceanic lithosphere, *Geophys. J. Int.*, **142**(3), 855–875.
- Wessel, P., 1992. Thermal stresses and the bimodal distribution of elastic thickness estimates of the oceanic lithosphere, *J. geophys. Res.*, **97**(B10), 14 177–14 193.
- Wessel, P., 1993. A reexamination of the flexural deformation beneath the Hawaiian Islands, *J. geophys. Res.*, **98**(12), 112–177.
- Wessel, P., 1996. Analytical solutions for 3-D flexural deformation of semi-infinite elastic plates, *Geophys. J. Int.*, **124**(3), 907–918.
- Wessel, P. & Smith, W.H., 1998. New, improved version of generic mapping tools released, *EOS, Trans. Am. geophys. Un.*, **79**(47), 579–579.
- Yamano, M. & Uyeda, S., 1990. Heat-flow studies in the Peru Trench subduction zone, in *Proceedings of the Ocean Drilling Program, Scientific Results*, pp. 653–661, eds Suess E., von Huene R. *et al.*, Ocean Drilling Program, College Station, TX.
- Yoshii, T., 1979. A detailed cross-section of the deep seismic zone beneath northeastern Honshu, Japan, *Tectonophysics*, **55**(3), 349–360.
- Zhang, F., Lin, J. & Zhan, W., 2014. Variations in oceanic plate bending along the Mariana trench, *Earth planet. Sci. Lett.*, **401**(0), 206–214.
- Zhong, S. & Watts, A.B., 2013. Lithospheric deformation induced by loading of the Hawaiian Islands and its implications for mantle rheology, *J. geophys. Res.*, **118**(11), 6025–6048.
- Zoback, M.D. *et al.*, 1987. New evidence on the state of stress of the San Andreas fault system, *Science*, **238**(4830), 1105–1111.

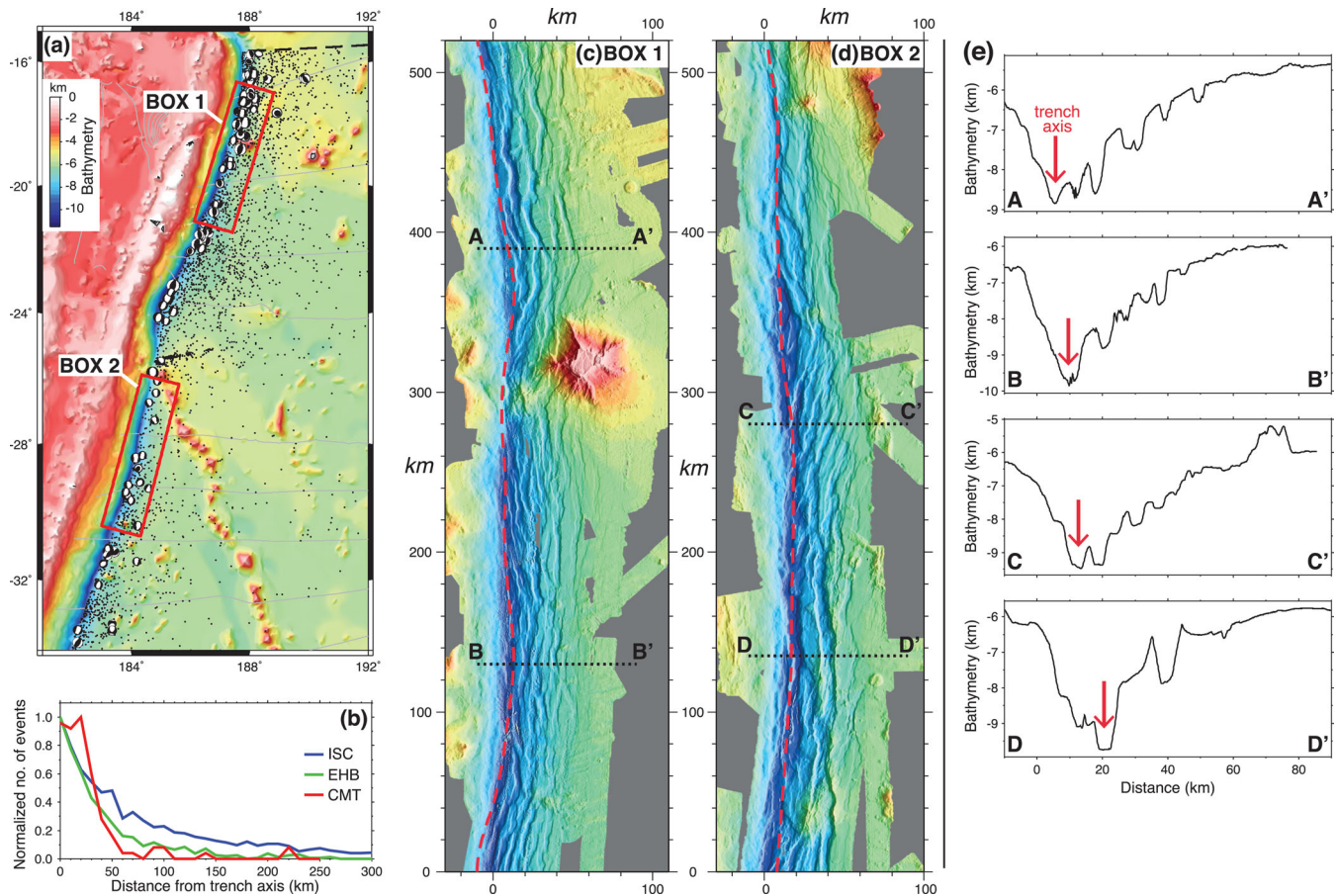


Figure A1. Plots showing seismicity and bend-faulting at the outer trench-slope of the Tonga-Kermadec trench. (a) GEBCO bathymetry overlain with all earthquakes, as of 2013, in the ISC (black dots) and CMT (focal mechanisms) catalogues. Only events seaward of the trench axis and within the trench-bin (black dash) are shown. CMT events have been plotted at their respective EHB positions, as these are more accurate (e.g. Bürgmann *et al.* 2005). (b) Histograms of ISC, EHB and CMT seismicity against distance from the trench, where the bin width is 10 km. This shows a landward increase in seismicity due to bend-faulting on the outer trench-slope. (c, d) Swath bathymetry, gridded at 200 m resolution, from the boxes shown in Fig. A1(a). This is from a newly compiled, cleaned data set comprised of all available data in the region, totalling 36 cruises. The incoming fabric of oceanic crust strikes at high angles to the trench and therefore new, large-offset, horst-and-graben style faults are formed. (e) Swath bathymetry along the profiles shown in Figs A1(c) and d. This shows the horst and graben structures, which are bounded by bend-faults with offsets up to >1.5 km.

APPENDIX A: SWATH BATHYMETRY OF THE OUTER TRENCH-SLOPE SEAWARD OF THE TONGA-KERMADEC TRENCH

In order to better evaluate the region of weakening in the outer trench-slope, we have used data from 36 swath bathymetry cruises to construct a new, fully cleaned, 200×200 m bathymetry grid of the Tonga-Kermadec trench-outer rise region (Fig. A1). Here, the incoming tectonic fabric of oceanic crust strikes approximately perpendicular to the local trench axis. As a result, the fabric is difficult to reactivate and so new, trench-parallel, large-offset (up to >1.5 km) and widely spaced (~ 5 – 10 km) normal faults are formed as the plate flexes into the trench (Fig. A1). Both landward-dipping and seaward-dipping faults are formed such that they bound horst and graben structures. This contrasts with subduction zones where the fabric of oceanic crust strikes at low angles to the trench (<25 – 30°) and is reactivated as a series of small-offset (150–500 m), closely spaced (a few km), landward-dipping faults (e.g. Massell 2002; Ranero *et al.* 2003; Billen *et al.* 2007). Fig. A1(b) show that bend-faulting at the Tonga-Kermadec trench is coincident with a landward increase in seismicity.

APPENDIX B: BATHYMETRY POWER SPECTRA AND SYNTHETIC NOISE PROFILES

We wished to add noise to our synthetic profiles that is representative of that in our observed ensemble-averaged profiles. We therefore conducted a spectral analysis of ensemble-averaged profiles of bathymetry (GEBCO One Minute, v2.0; Ioc *et al.* 2003) that are coincident with our circum-Pacific gravity profiles. We analysed 800-km-long profiles that extend 500–1300 km seaward of the trench axis in order to exclude the long-wavelength trench-outer rise flexural signal. The power spectrum for each segment-bin ensemble-averaged bathymetry profile was estimated using the periodogram, and these were then averaged within each subduction zone to reduce the variance.

Fig. B1 shows the average power spectrum for each subduction zone. The log-log spectra are not well fit by a straight line, and thus the ensemble-averaged bathymetry does not have fractal geometry, in contrast to individual ship track data (e.g. Bell 1975; Mareschal 1989). The rapid falloff in power at shorter wavelengths is likely because much of the short-wavelength information has been removed by the ensemble-averaging process.

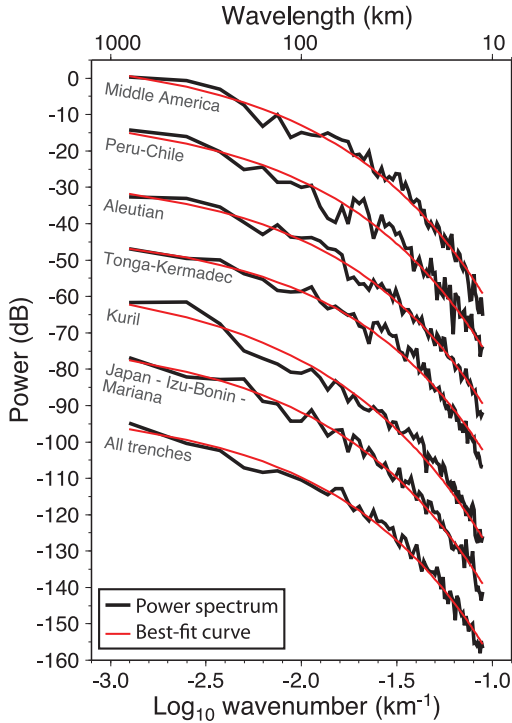


Figure B1. Average power spectrum estimates (black lines) for abyssal ensemble-averaged bathymetry seaward of circum-Pacific subduction zones. Best-fitting curves are shown in red; the equation that defines these curves was used in the generation of the synthetic noise profiles.

Trial and error reveals that the power spectra are well fit by an equation of the form:

$$\log(P) \propto A.10^{B\log(f)},$$

where P is power, f is wavenumber, and A and B are constants. With A held fixed at -25 , least squares regression gives a mean best-fitting value for B of 0.55 ± 0.02 . This equation and these best-fitting values were then used to generate synthetic bathymetric noise using a modified version of the spectral synthesis method of Peitgen *et al.* (1988), where the amplitude of the noise was scaled to represent that in our observed ensemble-averaged profiles.

APPENDIX C: DERIVING T_e AND PLATE CURVATURE AT THE HAWAIIAN ISLANDS

In order to use our YSE-based approach to constrain mantle rheology at the Hawaiian Islands, we first required an estimate of the ‘observed T_e ’. We modelled seismically constrained depths to the top of the oceanic crust (Watts & ten Brink 1989) that were acquired along three ridge-normal ship-tracks that intersect the Hawaiian chain between the islands of Oahu and Molokai (white points in Fig. C1a; coloured points in Fig. C1c). The data were corrected for swell topography, thermal age and local changes in crustal thickness (Zhong & Watts 2013).

The data were modelled using a 3-D elastic plate acted on by a volcanic load (black in Fig. C1b) that was isolated from the observed bathymetry (Fig. C1a; grey dash in Fig. C1b) using the 4500 m isobath that surrounds the Hawaiian chain. We assumed that the material directly beneath the load has the same density as the load and the material in the surrounding flexural moats has density 2300 kg m^{-3} , which is representative of a mix of

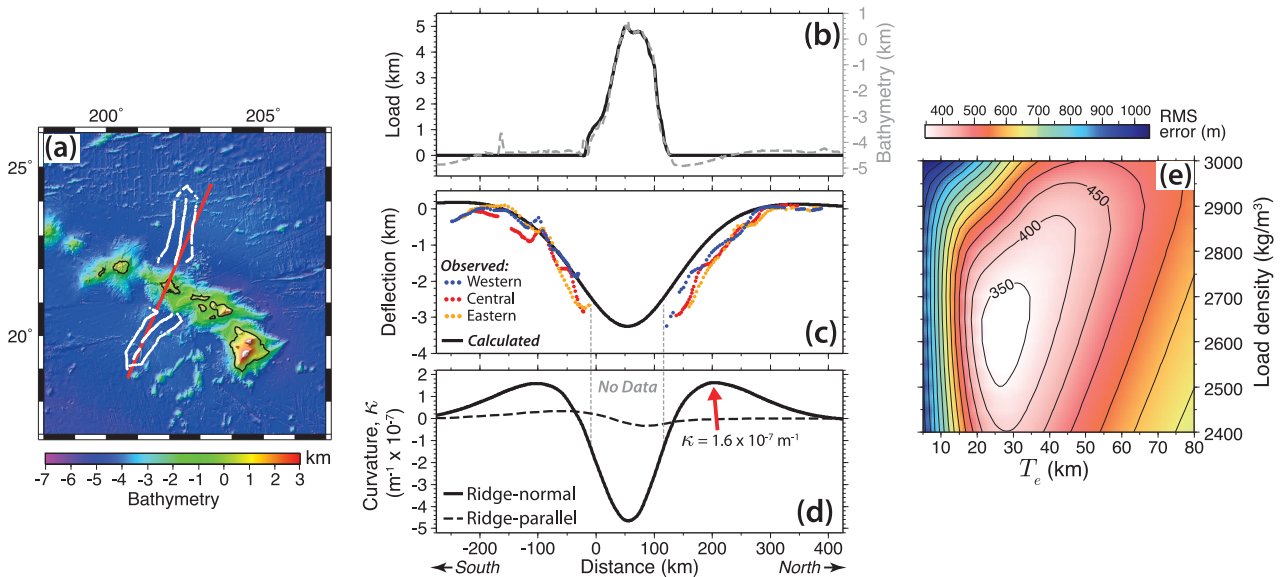


Figure C1. Results from flexural modelling at the Hawaiian Islands. (a) Bathymetry (GEBCO_08 30×30 second, Ioc *et al.* 2003). The major islands are shown in black, and the white points are the locations of seismically constrained crustal deflections collected along three ship transects by Watts & ten Brink (1989). (b) Observed bathymetry (grey dash) and the load used in the 3-D flexure calculation (black), sampled along the red profile in Fig. C1(a). The load was isolated from the observed bathymetry using the 4500 m isobath that surrounds the Hawaiian chain. (c) Observed seismically constrained crustal deflections (Watts & ten Brink 1989) projected along the red profile in Fig. C1(a) and the best-fitting calculated deflection along the same profile. (d) Ridge-normal and ridge-parallel curvature of the best-fitting elastic plate model, sampled along the red profile in Fig. C1(a). The predicted T_e was calculated using the maximum ridge-normal curvature in the regions where we have observed data. (e) RMSE between the observed and calculated crustal deflections as a function of T_e and load density.

volcanolastic and pelagic sediments. The best-fitting T_e and load density were found using a grid-search inversion technique (Fig. C1e). T_e and density were iterated in steps of 1 km and 50 kg m⁻³, respectively, the program of Cardozo (2009) was used to calculate the 3-D plate flexure, and a damped least-squares algorithm was used to find the best-fitting vertical shift in the calculated flexure.

Fig. C1(e) shows that there is a well-defined minimum in the RMSE, with best-fitting T_e and load density of 26 km and 2600 kg m⁻³, respectively. The T_e is in agreement with previous flexure studies (Watts 1978; Wessel 1993) and the density is compatible with density measurements from basalts at the Hilo drill hole on Hawaii (Moore 2001). Fig. C1(c) shows the best-fitting flexure (black) along the red profile in Fig. C1(a), and the observed crustal deflections (coloured points) projected along the same profile. This shows that the best-fitting elastic plate model provides a good fit to the observations, but that the deflection is underestimated to the

north of the islands. This was also found with the finite-element viscoelastic model of (Zhong & Watts 2013), so it is not a result of using a simple elastic plate model. It has been suggested that it may be a result of a break in the plate (Wessel 1993) and/or flexural deformation (Watts & ten Brink 1989) at the Molokai fracture zone.

After calculating the observed T_e , we required an appropriate value of plate curvature to calculate the predicted T_e . As is shown in Fig. C1(d), we used the maximum ridge-normal plate curvature of the best-fitting model along the red profile in Fig. C1(a), excluding the region where there is no data. We also conducted tests using the maximum curvature in the region with no data coverage and it makes little difference to the results. Fig. C1(a) also shows that the ridge-parallel plate curvature along the same profile is relatively low ($<0.3 \times 10^{-7} \text{ m}^{-1}$), and therefore it was reasonable to assume plane strain when calculating the predicted T_e using our YSE-based approach.